J Mater Sci (2017) 52:11851–11890

Mechanochemical Synthesis

Chalcogenide mechanochemistry in materials science: insight into synthesis and applications (a review)

P. Baláž[1], M. Baláž[1,*], M. Achimovičová[1], Z. Bujňáková[1], and E. Dutková[1]

[1] *Institute of Geotechnics, Slovak Academy of Sciences, Košice, Slovakia*

Received: 29 January 2017
Accepted: 4 May 2017
Published online: 24 May 2017

ABSTRACT

The aim of this paper on recent development in chalcogenide mechanochemistry is to provide a comprehensive review of advances achieved in the field of mechanochemical synthesis of nanocrystalline binary, ternary and quaternary chalcogenides and their nanocomposites. The synthetic approaches from elements and compounds are reviewed. The current focus of mechanochemical synthesis is on materials with potential utilization in future. In order to demonstrate the suitability of mechanochemically prepared chalcogenides for various applications, the concrete examples of the utilization of these materials in materials engineering, bioimaging and cancer treatment are provided. The possibility of scaling for industrial applications is also reviewed. The simplification of the synthesis processes with their reproducibility and easy way of operation, ecological safety and the product extraordinariness (nanoscale aspects) emphasizes the suitability of mechanochemistry application in chalcogenide synthesis.

Introduction

Mechanochemistry today belongs to vital branches of chemistry with many applications outside natural sciences. Materials science and technology is an outstanding example. The diversified fields of application can be illustrated by topics treated in number of mechanochemical conferences arranged across the globe in recent years. International Symposia on Mechanochemistry in 2015 (Montpellier-France and Hefei-China) and I. International Symposium on Mechanochemical Synthesis and Reactions in Materials Science as part of the huge Materials Science & Technology Conference organized in 2016 in Salt Lake City, USA, are good examples. IX. International Conference on Mechanochemistry and Mechanical Alloying, which will be held in 2017 in Košice, Slovakia, is currently under preparation. The research activities can be identified in a number of exciting review papers published in the last decade [1–25].

Chalcogenides, as advanced perspective materials, exhibit a great variety of properties tunable via

Dedicated to the memory of Professor Eberhard Gock.

Address correspondence to E-mail: balazm@saske.sk

DOI 10.1007/s10853-017-1174-7

mechanochemical treatment. They represent unceasing application possibilities in material science (Table 1). It is the aim of this review paper to illustrate the progress in chalcogenide mechanochemistry in the last decenary. The focus is devoted to the mechanochemical synthesis of these compounds and various fields of their application.

Mechanochemical synthesis

In this paper, we will focus on two types of mechanochemical solid-state synthesis (Fig. 1).

Synthesis from elements (Fig. 1a) is usually running in dry mode and inert atmosphere (nitrogen, argon), preventing in situ and/or post-treatment solid–gas reactions. If mechanochemical synthesis is applied in the presence of air oxygen, the first surface layers of the treated solids are degraded to some extent [26]. In case of sulphides, a great variety of different species can be created on their surface like sulphates, hydroxysulphates, oxysulphates, thiosulphates, sulphites, hydroxides, hydroxyoxides or oxides [27].

Wet mode of synthesis usually utilizes advantages of wet milling which are being applied in mechanical activation of solids for a long time to produce finer and more homogeneously dispersed particles [1, 27]. For mechanochemical synthesis of chalcogenide nanocrystals, the so-called acetate route (Fig. 1b) has been developed in 2003 [28].

The advantage of the acetate route lies in two peculiarities:

1. Both precursors used in the synthesis (acetate and sulphide) contain crystalline water, which is liberated at the beginning of the mechanochemical synthesis. After the liberation of water from their structure, the dangling bonds of the precursors are exposed and, as a consequence, are very reactive, and product can be synthesized in a short time at ambient conditions [27, 29–41].
2. The by-products of the wet mechanochemical synthesis are water-soluble, and the whole synthetic procedure needs only several simple additional operations like washing, decantation and drying. The size of the obtained nanocrystals is in nanorange, the prepared nanocrystals are homogeneously distributed and, in comparison with the dry mode of synthesis, they have well-developed surface area, which is usually one order higher than when the dry synthesis from elements is applied. This broadens spectrum of their applications, e.g. in the areas such as catalysis and adsorption.

Binary chalcogenides

Synthesis from elements

Sulphides Bi_2S_3 Mechanochemical synthesis of nanocrystalline sulphide semiconductor Bi_2S_3 from elements using high-energy milling in a planetary laboratory mill has been investigated [42]. Bismuth sulphide is an attractive material for photoelectrochemical applications, as it has a reasonably narrow band gap ($E_g = 1.3$ eV). It is also a promising semiconductor material for applications in photovoltaic cells and thermoelectric cooling technologies, because of its environmental compatibility. Structural and microstructural characterization of the prepared particles, including phase identification, specific

Table 1 Chalcogenides in materials science

Chalcogenide	Application
$CuInS_2$, $CuInSe_2$, Cu_2ZnSnS_4, $CuIn_xGa_{(1-x)}Se_2$	Solar energy conversion
ZnS, PbS, Ag_2S, CdSe	Infrared windows and detectors
PbS, CdS, BeZnSeTe, $CuInS_2$	Light-emitting diodes
FeS, Co_9S_8, MoS_2, WS_2, CoS_2	Hydrogen evolution and storage
$Cu_{12}Sb_4S_{13}$, CuS, CuSe, Cr_2S_3	Thermoelectricity
TiS_2, MoS_2, WS_2, NiS_2, GeS	Lithium- and sodium-ion batteries
ZnS:Mn, SrS:Ce, $BaAl_2S_4$:Eu	Luminescence
Ag_2S, PbS	Ion-selective electrodes
Cr_5S_6, $Fe_xMn_{1-x}S$, $Co_xMn_{1-x}S$	Giant magnetoresistors
CdS, CdSe, CdTe, Ag_2S	Diagnostics
MoS_2, Sb_2S_3, SnS, WS_2, FeS	Wear resistance
MoS_2, FeS, ZnS, RuS_2, WS_2	Catalysts

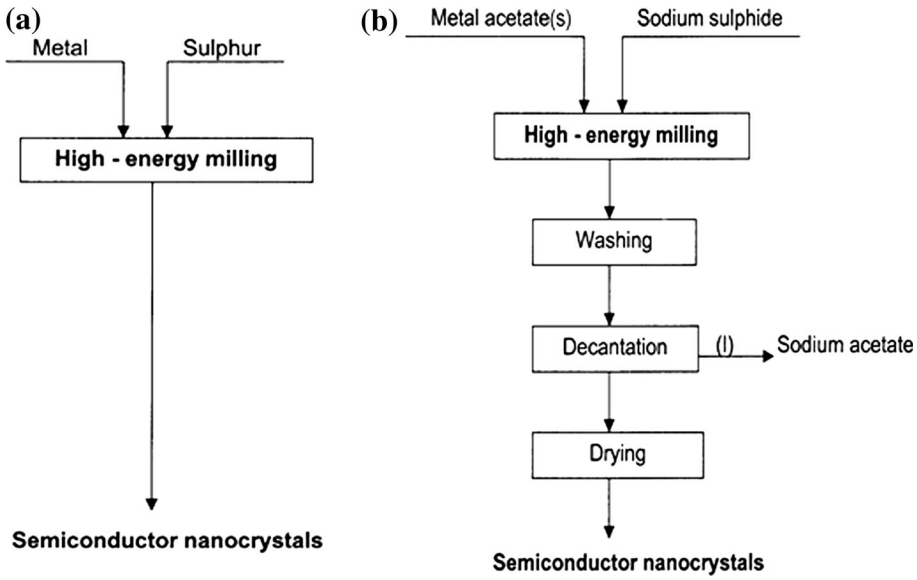

Figure 1 Mechanochemical synthesis of semiconductor nanocrystals: **a** dry mode, **b** wet mode.

surface area measurement and particle size analysis has been carried out. The optical properties were also measured by spectroscopic methods, and the structural stability up to 500 °C was studied by thermal analysis [43].

Nanocrystalline Bi_2S_3 particles were prepared according to the following equation:

$$2Bi + 3S \rightarrow Bi_2S_3 \quad (1)$$

The progress of the mechanochemical synthesis of Bi_2S_3 is illustrated in Fig. 2a by XRD patterns of the mixture of bismuth and sulphur precursors (1) and the sample milled for 60 min (2).

In the starting material (pattern 1), only peaks belonging to Bi (JCPDS 77-7112) and S (JCPDS 78-1888) can be seen. The mechanochemically synthesized Bi_2S_3 (bismuthinite) has the orthorhombic structure (space group 62, P_{nma}), with the refined lattice parameters $a = 11.3008$ Å, $b = 3.9855$ Å and $c = 11.1439$ Å. The estimated average crystallite size, D, is 26 nm. The process is rather straightforward, with Bi_2S_3 (JCPDS-74-9437) being the only solid product (pattern 2). The surface morphology was investigated by SEM (Fig. 2b). Bi_2S_3 aggregated particles with irregular morphology were obtained. The size of the particles is rather uniform with an average hydrodynamic diameter of 198 nm, which was determined by the photon cross-correlation spectroscopy, as shown in Fig. 2c. The size dispersion is relatively narrow, with unimodal distribution profile.

The absorption UV–Vis spectrum of the Bi_2S_3 (Fig. 3a) shows a weak absorption peak at ~280 nm. The band gap is determined from intercept of the extrapolated linear fit to the experimental data of the Tauc plot. A band gap of 4.5 eV was estimated by extrapolating the linear part of the graph as shown in Fig. 3a (inset). It is quite similar to that synthesized by other authors [44]. The observed peaks are blue-shifted relative to the bulk Bi_2S_3 at 956 nm (1.3 eV) [45] and are assigned to the optical transitions of the excitonic states of Bi_2S_3. The obvious blueshift could be attributed to the existence of very small Bi_2S_3 nanocrystalline particles agglomerated into large clusters.

Room-temperature PL spectrum with the excited wavelength at 325 nm is shown in Fig. 3b. The corresponding emission peaks at 490 nm (2.51 eV) and 390 nm (3.18 eV) could be observed for the Bi_2S_3 nanoparticles. They can be ascribed to a high-level transition in Bi_2S_3 semiconductor nanocrystallites. This kind of band edge luminescence can arise from the recombination of excitons and/or trapped electron–hole pairs, whereas PL background could be assigned to the surface-assisted radiative recombinations in sulphide nanocrystallites of varying size [46]. In paper [47], further application potential of this sulphide has been studied by measuring its thermoelectrical properties.

Sb_2S_3 Antimony sulphide, Sb_2S_3, is a semiconductor material with high photosensitivity and high thermoelectric power. Sb_2S_3 fulfils the optical requirements to obtain an electronic band gap in the visible or the near-infrared (NIR) region, depending on its

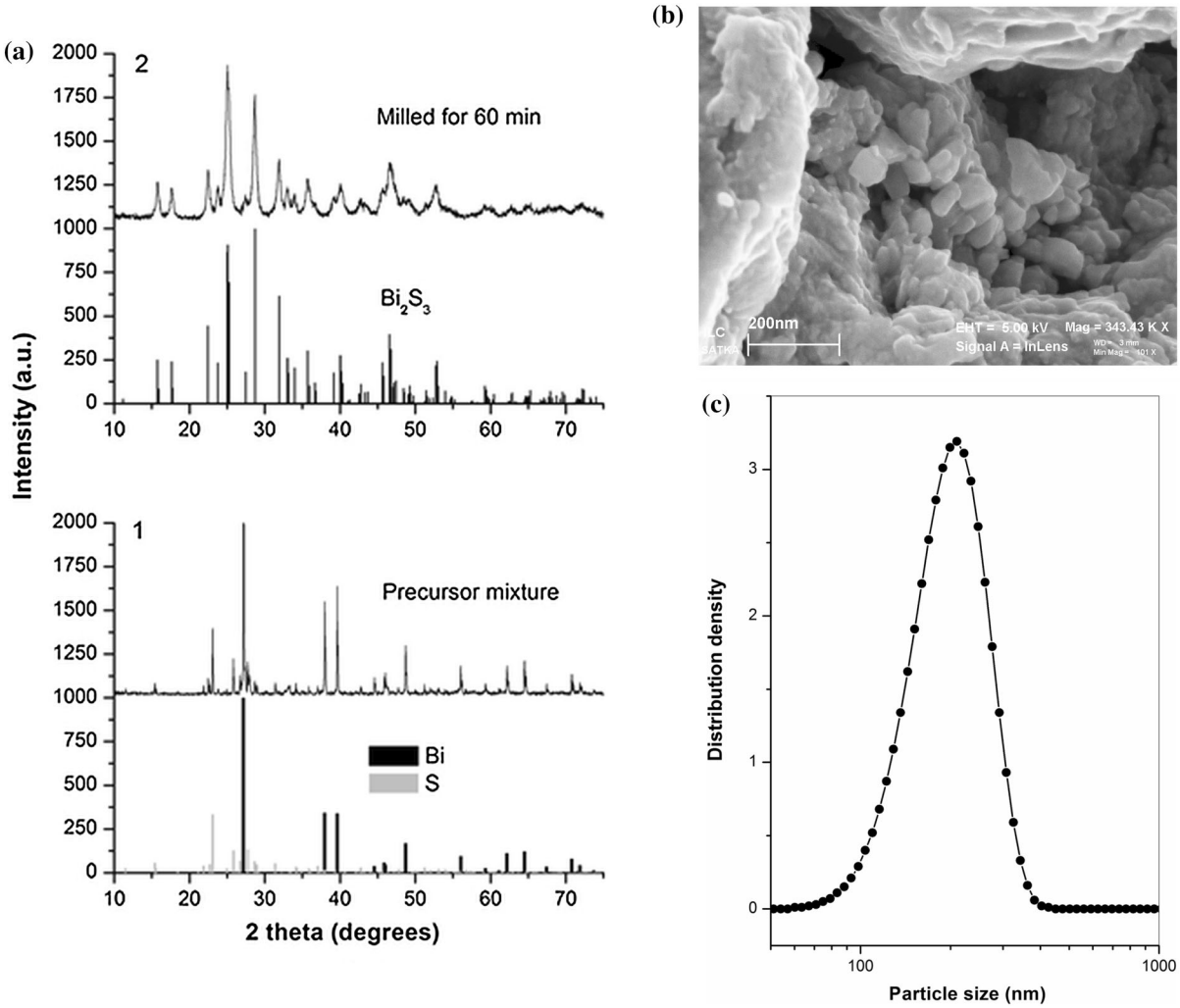

Figure 2 **a** X-ray diffraction patterns, **b** SEM and **c** particle size distribution of the Bi_2S_3 nanoparticles synthesized after 60 min of milling. Reprinted with permission from Ref. [43]. Copyright 2014, Elsevier.

amorphous or crystalline nature. The electronic gap lies around 2.2 eV (564 nm) for amorphous and 1.78 eV (697 nm) for crystalline Sb_2S_3 thin films. The preparation and kinetics of mechanochemical synthesis of Sb_2S_3 nanoparticles obtained by high-energy milling of elements were studied in paper [42]. The detailed structural and microstructural characterization of the mechanochemically synthesized Sb_2S_3 after 60 min from the possible application point of view was studied in paper [48].

Nanocrystalline Sb_2S_3 particles were synthesized according to the following reaction:

$$2Sb + 3S \rightarrow Sb_2S_3 \quad (2)$$

The Sb_2S_3 sample obtained after 60 min of milling was analysed as well by ED, TEM, HRTEM and EDS techniques, and the obtained results are depicted in Fig. 4. The powder sample is composed of the agglomerated particles, as shown in the TEM image (Fig. 4a). The corresponding ED (inset) is a ring pattern, indicating the small diffraction domain of the crystals; all the rings were indexed (the (*hkl*) planes are marked in the figure) in the orthorhombic system of the Sb_2S_3 sample with P_{nma} space group. The energy-dispersive X-ray spectrum (EDS) (Fig. 4b) shows that the synthesized material is pure antimony sulphide with no detectable impurities; Cu and C peaks are coming from the grid. The elemental semiquantitative analysis indicates the Sb/S atomic ratio of 2/3 which is in good agreement with the formula. The HRTEM technique reveals that the particles are formed by small nanocrystals of different sizes. Only a few nanocrystals with really small size (about 5 nm) were found, and one of them is

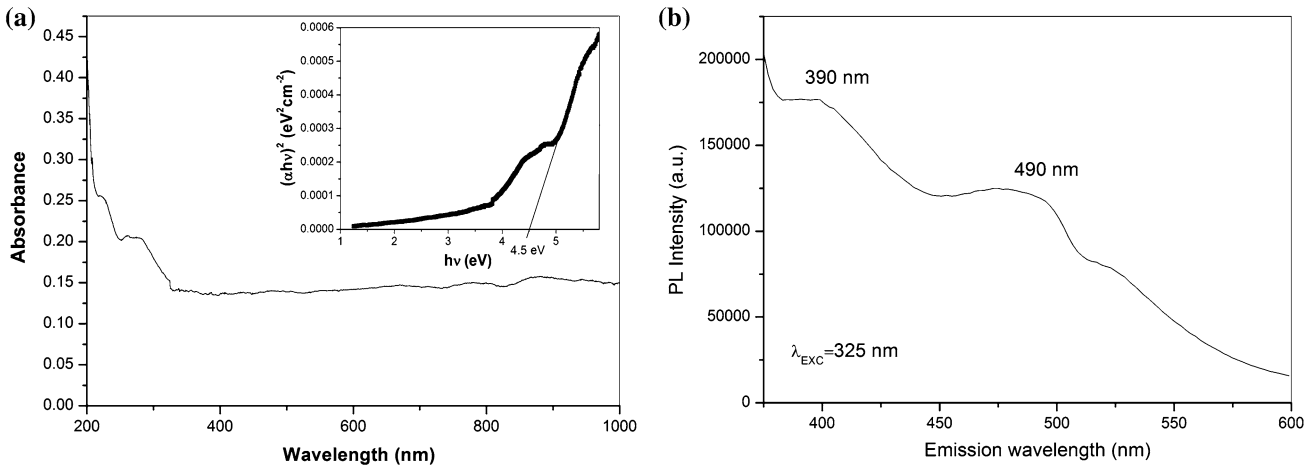

Figure 3 **a** UV–Vis absorption (variation of $(\alpha hv)^2$ vs. hv is shown in *inset*) and **b** photoluminescence spectrum of the Bi_2S_3 synthesized after 60 min of milling. Reprinted with permission from Ref. [43]. Copyright 2014, Elsevier.

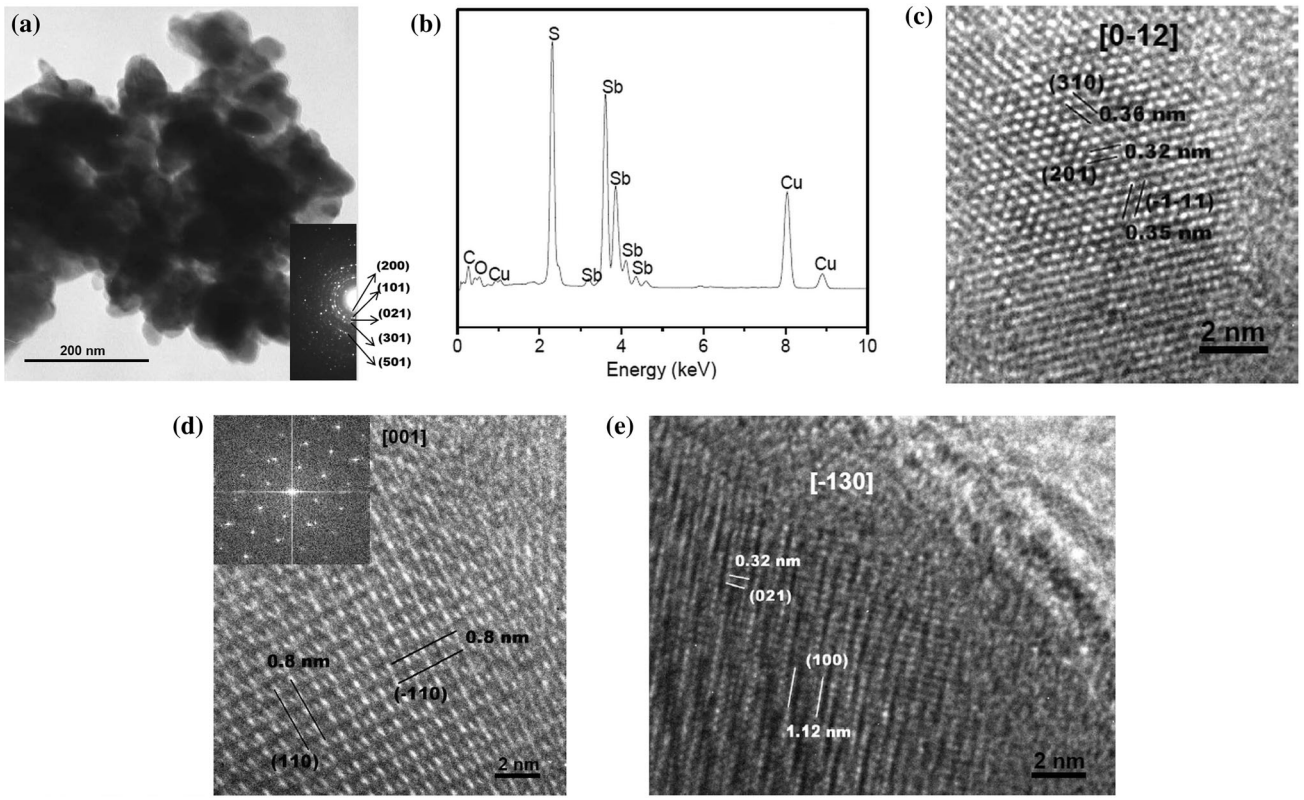

Figure 4 Microstructure of the Sb_2S_3 sample obtained after 60 min of milling: **a** TEM micrograph and the corresponding ED ring (*inset*); **b** EDS spectrum; **c**–**e** HRTEM micrographs. Reprinted with permission from Ref. [48]. Copyright 2014, Elsevier.

presented in Fig. 4c. The presented nanocrystal is oriented along the [0–12] zone axis, and the corresponding interplanar spacing is marked. The majority of the nanocrystals were larger (about 20 nm). Figure 4d shows a crystalline nanodomain oriented along [001] zone axis, and the fast Fourier transform (FFT) image in the inset reveals very good periodicity of the nanocrystals. Figure 4e presents a nanocrystal nearly oriented along [−130]. The interplanar spacing and (*hkl*) planes are also marked. The average crystalline nanodomain size found for Sb_2S_3 (∼20 nm) is in good agreement with the XRD result, and it is

higher than for Bi_2S_3 (5–10 nm) [43]. The particle size measured by the photon cross-correlation spectroscopy presents a similar tendency: about 210 nm for Sb_2S_3 and 198 nm for Bi_2S_3.

Figure 5a shows the DSC curve obtained for the Sb_2S_3 mechanochemically synthesized for 60 min. The first run shows an endothermic peak at about 100 °C due to the loss of adsorbed water and a broad exothermic peak between 200 and 300 °C that can be related to the processes of recovery and recrystallization of the defects generated during milling. The second and third runs show also a weak exothermic peak. Figure 5b shows the XRD patterns of the same sample before (Fig. 5b1) and after (Fig. 5b2) heating to 500 °C during the DSC measurement. When this sample is heated in the calorimeter, the corresponding X-ray diagram shows the same peaks but quite narrow and well resolved. This is an evidence of good crystallinity, resulting from the processes indicated by the peak at 290 °C in the DSC diagram. The estimated crystallite size after the three DSC cycles increased 23-fold to about 827 nm.

Interesting aspect of binary sulphides synthesis is combination of mechanical milling and electric discharge (EDAMM process). Bi_2S_3 and Sb_2S_3 were synthesized by this method, and particles in microrange were documented [49].

The mechanochemical synthesis of the nanocrystalline Bi_2S_3 and Sb_2S_3 particles from corresponding metal and sulphur powders by high-energy milling is a suitable system for a large-scale mechanochemical preparation.

Cu–S Copper sulphides represent interesting group of semiconductor materials, because they can be present in many different stoichiometries, ranging from Cu-rich chalcocite, Cu_2S, to sulphur-rich villamaninite, CuS_2. Probably, the most common compound is covellite, CuS. Between Cu_2S and CuS, several non-stoichiometric forms exist, concretely yarrowite $Cu_{1.12}S$, spionkopite $Cu_{1.39}S$, geerite $Cu_{1.6}S$, anilite $Cu_{1.75}S$, digenite $Cu_{1.8}S$ and djurleite $Cu_{1.96}S$. Most of these compounds are present in nature as minerals [50]. The application of copper sulphides in general is quite multidisciplinary, as can be traced down in the recent literature [51, 52], namely their utilization as a photothermal agent in biomedical applications is gaining interest [53, 54]. There are multiple ways of copper sulphide preparation, starting from classical chemical approaches like hydrothermal/solvothermal synthesis, sol–gel method or hot injection method, as recently reviewed in [51]. However, also mechanochemistry has an inevitable place in the synthesis of copper sulphides. They can be synthesized using elemental precursors or various compounds. The starting materials have a crucial influence on the properties of the final product. The synthetic process can take from minutes to hours, depending on the milling conditions and materials used. In Table 2, the papers dealing with the preparation of copper sulphides from elements

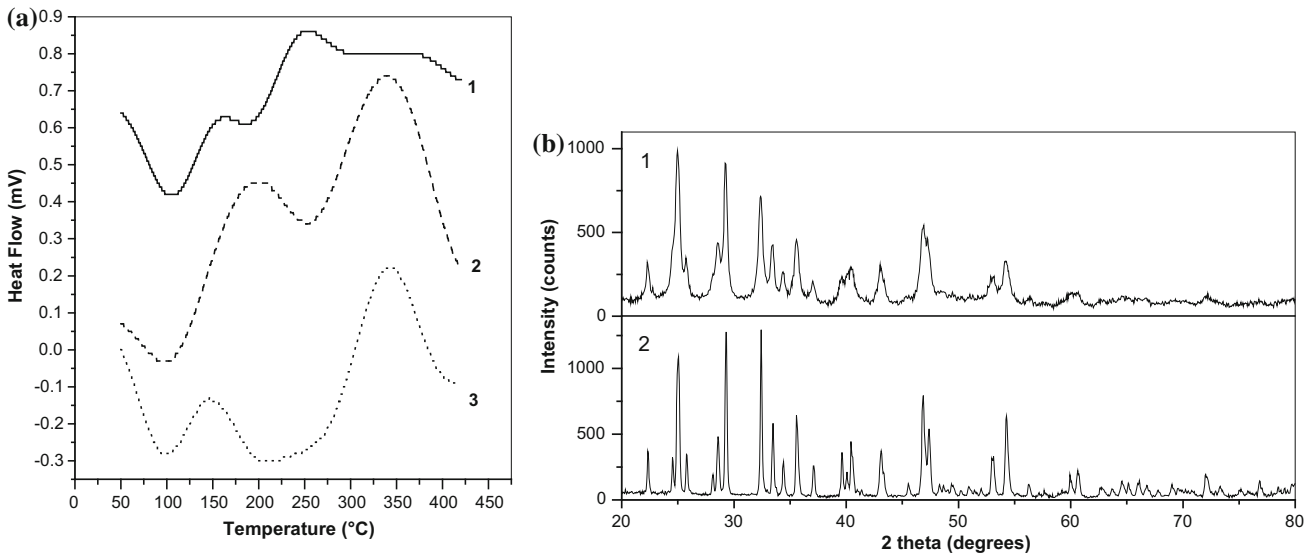

Figure 5 **a** DSC diagram (*1*—run 1, *2*—run 2 and *3*—run 3) and **b** XRD patterns of mechanochemically synthesized Sb_2S_3 for 60 min before DSC measurements (*1*) and after DSC measurements (*2*). Reprinted with permission from Ref. [48]. Copyright 2014, Elsevier.

Table 2 Mechanochemical approaches for the synthesis of copper sulphides from elements

Reaction time (min)	Material of milling media	Atmosphere	Products	Ref.
1200	Agate	$Ar/N_2/CO_2$	Cu_xS	[55]
60–120	Agate	Air	Cu_xS	[56]
120	WC	Ar	Cu_2S	[57]
10	Steel	Ar	CuS	[58]
15	WC	Air	CuS	[59]
20	ZrO_2	Not stated	CuS, $Cu_{2-x}S$	[60]
120	Steel	Ar/H_2	CuS	[61]

using mechanochemistry, together with some experimental conditions are listed.

The synthesis times in all the reported cases were longer than 10 min. Very recently, our research group has used elementary precursors for the mechanochemical synthesis of copper sulphides, concretely stoichiometric compounds covellite and chalcocite, within a second range [62], according to reactions:

$$Cu + S \rightarrow CuS \quad (3)$$

$$2Cu + S \rightarrow Cu_2S. \quad (4)$$

It was found out that the morphology of the starting materials plays a crucial role in the course of the reaction pathway. Concretely, the morphology of copper was decisive. The needle-like morphology seemed more reactive, and it was confirmed for the studied system. Sulphur morphology did not seem to have such an effect. Depending on copper used, different events happened in the mill. In the case when electrolytic copper was used, the explosion was observed, as documented by the gas pressure and temperature changes in the milling chamber (Fig. 6a, b). When different kinds of copper (non-electrolytically prepared one) were used, no explosion during the first 5 min of milling was observed (Fig. 6c, d).

If the explosion took place (a, b), it always happened within the first 15 s of milling. In non-explosive reactions (c, d), only linear increase of temperature and pressure was observed. In order to investigate the progress of the reaction in the explosive and non-explosive mixtures, the XRD patterns were recorded (Fig. 7).

It can be clearly seen that in the case of electrolytical copper (Fig. 7a, b), copper sulphide with no signs of sulphur or copper was obtained. It has to be noted that the phase was not pure covellite, also some amount of non-stoichiometric digenite was found. In the case of non-electrolytical copper (Fig. 7c, d), the XRD patterns have shown a significant amount of both elemental precursors even after 5 min of milling. Four types of copper (two electrolytical and two differently prepared) and two types of sulphur were analysed altogether, and the observations were confirmed for all combinations. The results were similar also for the chalcocite formation.

It was concluded that if the reaction between copper and sulphur is performed in the explosive manner, the desired products in the form of nanoparticles can be formed within a second range [62]. Nevertheless, the explosion on a large scale needs to be controlled. We hypothesize that one of the main driving parameters of the explosion is the presence of air, so the reactions under argon also need to be investigated; however, they will most probably not proceed so quickly then.

As future perspectives, the synthesis of non-stoichiometric copper sulphides and the capping of the prepared compounds by a biocompatible organics using tools of mechanochemistry, in order to prepare nanosuspensions applicable in biomedicine, can be outlined. As potential capping agents, which have already been successfully applied, cysteine [63] or folic acid [64] can be mentioned. Copper sulphides possess high potential and are currently in the spotlight of researchers.

Other sulphides The synthesis of binary sulphides from elements exhibits several phenomena, which were treated from theoretical, as well as from application aspects. Among them, mechanically induced self-propagating synthesis, and a tendency of the products to aggregate are frequently discussed.

The explosive character of mechanochemical synthesis (as shown previously on the Cu–S system) has been studied extensively since the pioneering works of Bulgarian group [55, 65, 66]. A low-energy single-ball vibratory mill has been applied in this case [65]. Nowadays, Takacs in the USA and Urakaev in Russia

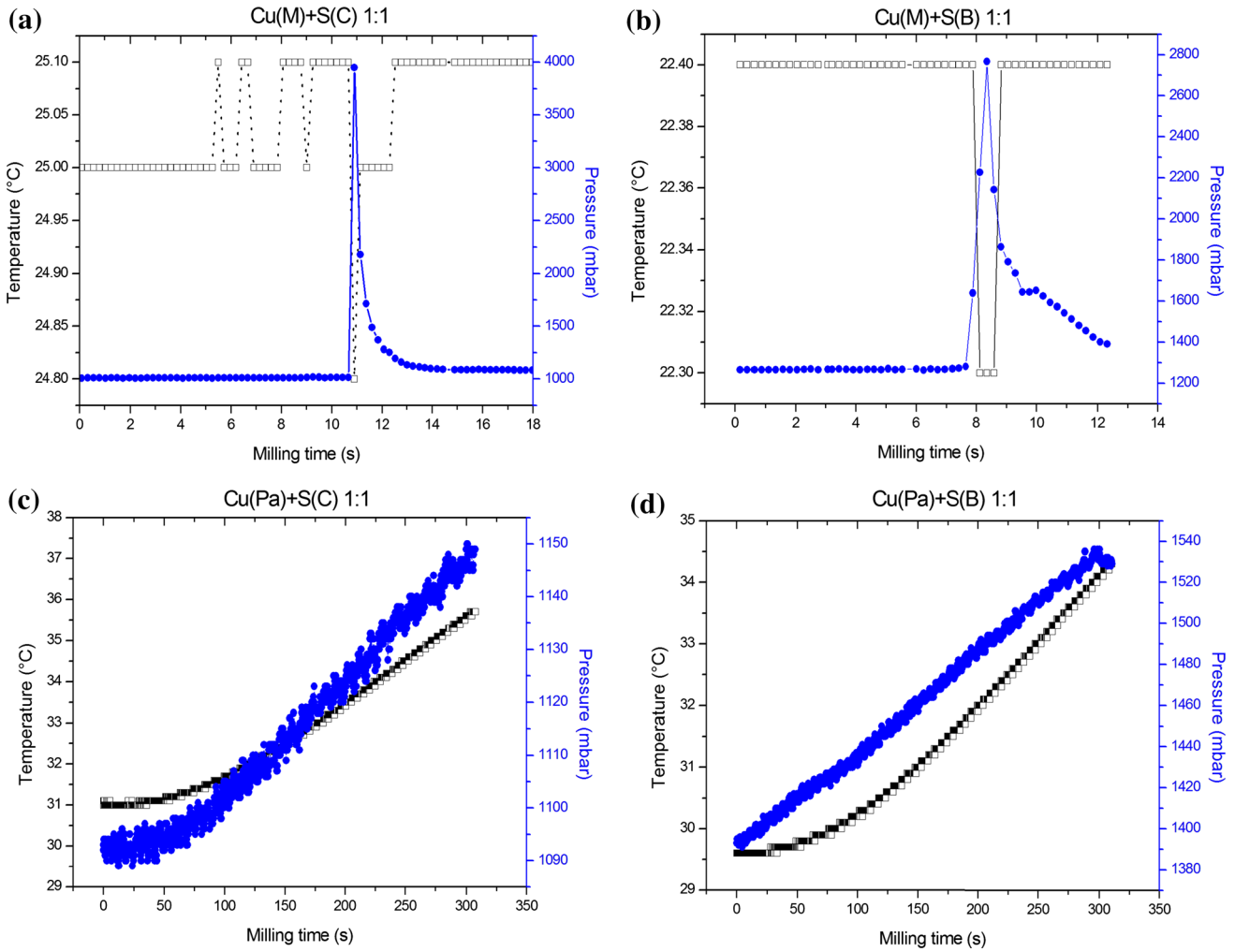

Figure 6 Gas pressure and temperature changes during milling. Cu(M)—electrolytically prepared copper, Cu(Pa)—copper prepared in the form of atomized powder, S(B), S(C)—sulphur from different producers. Time of milling: **a**, **b** until the explosion (approximately 10 s), **c**, **d** 5 min. Reprinted with permission from Ref. [62]. Copyright 2016, Royal Society of Chemistry.

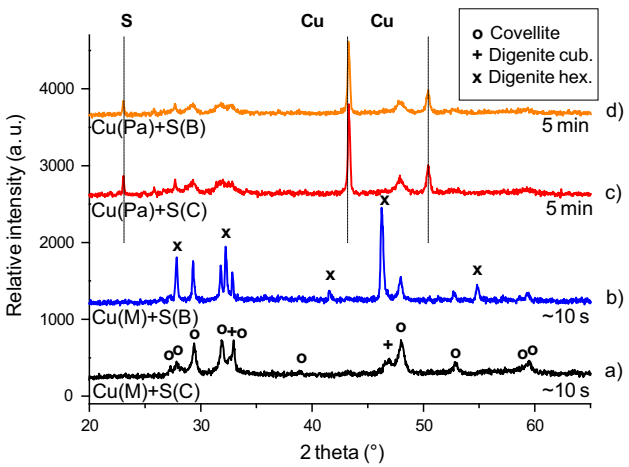

Figure 7 XRD patterns of the milled mixtures. Time of milling is given in figure. Reprinted with permission from Ref. [62]. Copyright 2016, Royal Society of Chemistry.

are the most prominent researchers in the field of explosive reactions of chalcogenides. Takacs published fundamental reviews [67, 68] and in his recent works [69, 70] mainly focused on zinc and tin selenides. The review paper elaborated by Urakaev concentrated on phenomenology, mechanism and kinetics of the mechanochemical synthesis in Zn–S–Sn and Zn–S systems, respectively [6, 18]. Zn–S system has been studied for a long time in previous decades [1, 27, 71]. However, new studies appeared recently, where spectroscopic techniques (optical, Raman) have been applied to describe mesoporous and quantum dots particles prepared by a mechanochemical synthesis [72–75]. The same techniques were applied also to characterize palladium chalcogenides [76].

The principal parameter of mechanically stimulated reaction for Zn–S system—the induction period of the ignition of combustion was numerically calculated taking into account the heat effects of chemical reactions. Later on, the author paid attention to changes of physicochemical properties of sulphur during high-energy milling, particularly to the anomalous increase in viscosity caused by its polymerization and tendency to be amorphous [77]. The effect of process control agents (ammonium chloride and stearic acid) was studied in order to disintegrate the agglomerated SnS_2 particles and improve the kinetics of its formation [78]. This material with layer structure seems to be attractive for Li-ion batteries, the primary energy storage system in modern electronics. In this case, the better crystallinity and the smaller particle size can positively influence the electrochemical performance. The good thermoelectric properties have been revealed in another tin system (SnS), the properties of which can be improved by combining the mechanochemical synthesis and spark plasma sintering [79]. The modification of other layer sulphides (MoS_2 and WS_2) by milling can find perspective application in heterogeneous catalysis [80, 81]. Elemental Mg and S powders were milled to prepare MgS in the work [82]. The biocidal effect against aerosolidized endospheres of *Bacillus thuringiensis* (simulant of *Bacillus anthracis*) was quantified. This is a good example of materials application in defence activities to defeat biological weapons.

Selenides Besides sulphides, also metal selenides belong to a group of semiconductors with applications in materials science. Optoelectronic applications for several purposes like blue-light-emitting diodes (ZnSe), laser diodes (ZnSe, BiSe, Bi_2Se_3), infrared detectors (PbSe, SnSe, $SnSe_2$), solar cells (ZnSe, $SnSe_2$, BiSe, Bi_2Se_3, CoSe), thermoelectric cooling materials (ZnSe, $SnSe_2$), ion-selective sensors (PbSe), photo- or electrocatalysts (CdSe, CoSe), topological insulators (Bi_2Se_3) and materials for lithium-ion batteries ($SnSe_2$, Bi_2Se_3) are very attractive [83]. These selected metal selenides were successfully prepared by a simple, fast and less-consumptive mechanochemical route in a laboratory planetary mill and an industrial vibratory mill, which have been proved as the effective reactors for their mechanochemical synthesis starting from the corresponding metal and selenium powders as the reaction precursors (Table 3).

Planetary ball mill Pulverisette 6 (Fritsch, Germany) was used for the mechanochemical synthesis of selected metal selenides. The particular examples will be shown below.

ZnSe, CdSe The X-ray diffraction patterns of mechanochemically prepared cubic ZnSe (stilleite, JCPDS PDF 37-1463) and cubic CdSe (JCPDS PDF 19-191) after 60 and 30 min of milling, respectively, are shown in Fig. 8. The morphology and nanocrystalline character of ZnSe were studied by TEM. The synthesized nanoparticles of size 10–20 nm form

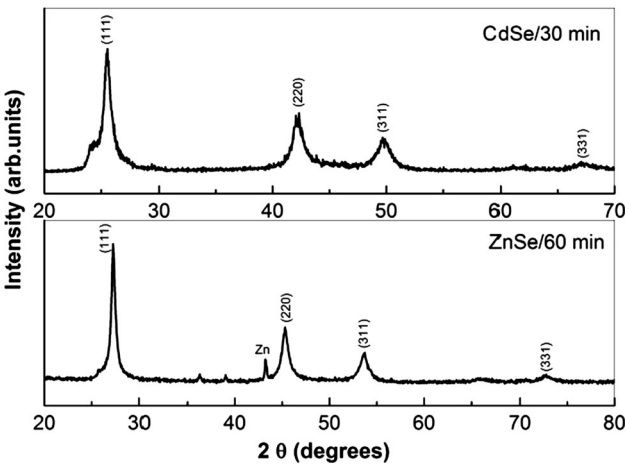

Figure 8 XRD patterns of CdSe and ZnSe, mechanochemically synthesized for 30 and 60 min, respectively.

Table 3 Mechanochemical approaches for the synthesis of metal selenides

Type of binary compound	Metal selenide	Solid-state reaction	ΔH^0_{298} (kJ.mol^{-1})
$A^{II}B^{VI}$	ZnSe	Zn + Se → ZnSe	−159.0
	CdSe	Cd + Se → CdSe	−144.8
$A^{IV}B^{VI}$	PbSe	Pb + Se → PbSe	−100.0
	SnSe	Sn + Se → SnSe	−88.7
$A^{IV}B_2^{VI}$	$SnSe_2$	Sn + 2Se → $SnSe_2$	−121.0
$A^{V}B^{VI}$	BiSe	Bi + Se → BiSe	−53.0
$A_2^{V}B_3^{VI}$	Bi_2Se_3	2Bi + 3Se → Bi_2Se_3	−140.0
$A^{VIII}B^{VI}$	CoSe	Co + Se → CoSe	−65.3

agglomerates (clusters) with size from 100 to 500 nm (Fig. 9a). However, also non-reacted selenium rods were detected. SAED rings also confirmed that ZnSe consists of very small particles and bigger ones distinguishable due to stronger reflections inside the diffraction rings (Fig. 9b). The existence of ZnSe nanoparticles was not confirmed through UV–Vis absorption spectroscopy, as smaller direct energy band gap of 2.27 eV was registered in comparison with characteristic band gap value 2.67 eV for bulk ZnSe [84]. It is probably a consequence of the agglomerates formation of mechanochemically synthesized ZnSe and unreacted needle-like selenium (see Fig. 9a), as the optical properties of semiconductors are strongly influenced by impurities and the structural defects. Photocatalytic properties of mechanochemically synthesized CdSe were tested for toluene and ethylene as the model air contaminants. The results showed that the photocatalytic activity of CdSe under UV irradiation reached only 5.8% ($\lambda = 365$ nm) and 9.6% ($\lambda = 254$ nm) conversion of ethylene compared to TiO_2 Degussa P25, whose photocatalytic activity reached 15.2 and 40.1% conversion, respectively. However, CdSe displayed a considerable photocatalytic activity with visible light (ethylene conversion degree 23.2%), while TiO_2 is inactive [85].

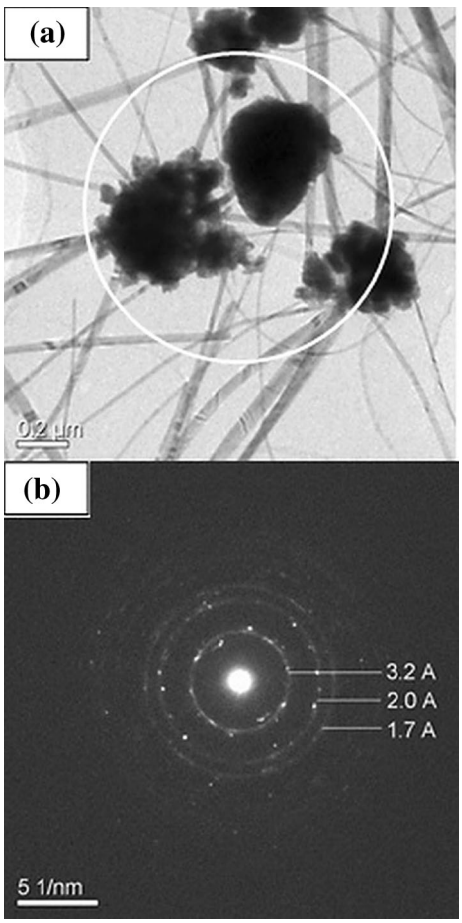

Figure 9 **a** TEM image of agglomerated ZnSe nanoparticles with needle-like selenium, **b** SAED pattern taken from the encircled area.

Both these systems were permanently studied by various authors, as can be traced down in the recent literature. Tan reported mechanochemical synthesis of CdSe already in 2009 [86]. The different CdSe modifications were observed in dependence of milling time. While wurtzite structure (hexagonal) has been identified in the sample milled for 4 h, zinc blende structure (cubic) was characteristic for milling for 40 h. CdSe nanocrystals were thoroughly described in [87]. Permanent interest for this material comes from its application in electrical and optoelectronic devices [88, 89]. Mechanochemical synthesis of CdSe and ZnSe nanocrystal shows signs of self-propagating reactions and was continually studied in either gradual or self-propagating mode [88, 90].

PbSe, SnSe The mechanochemical synthesis of PbSe is relatively fast. The degree of conversion reached 94% after 10 min of milling and 100% after 15 min. The XRD pattern of synthesized PbSe is provided in Fig. 10, and the peaks correspond to cubic PbSe (clausthalite, JCPDS PDF 6-354). The study of PbSe morphology using TEM illustrated that most PbSe nanocrystals were easily separated from the agglomerates after ultrasonic de-agglomeration.

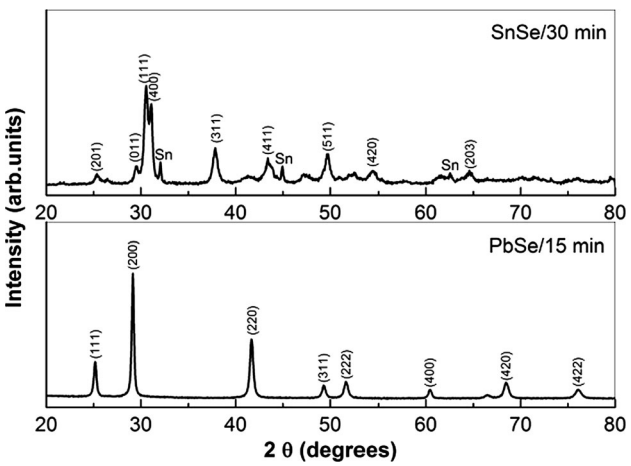

Figure 10 XRD patterns of SnSe and PbSe, mechanochemically synthesized for 30 and 15 min, respectively.

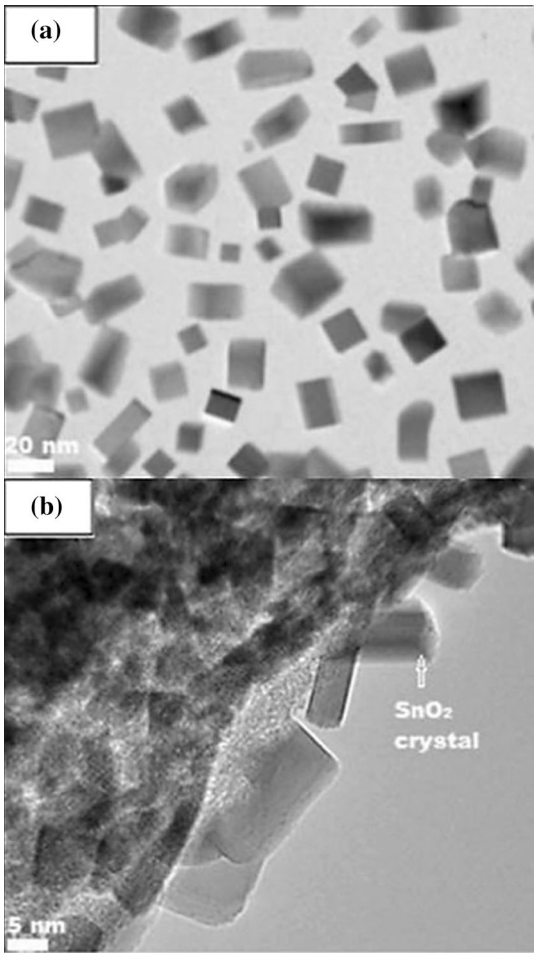

Figure 11 **a** TEM images of cubic PbSe nanocrystals, **b** TEM image of agglomerated plate-like SnSe nanocrystals with prismatic SnO_2 nanocrystals.

Idiomorphic PbSe nanocrystals have a cubic crystallographic form (Fig. 11a) and size ranging from a few up to 80 nm, whereby the average crystallite size 40 nm is consistent with the value 37 nm calculated from the XRD data. UV–Vis–NIR absorption spectrum of PbSe after 15 min of milling showed an extended absorption edge at ~1032 nm corresponding to 1.2 eV. This confirmed the expected size-dependent effect of quantum confinement with the blueshift from the direct band gap energy of 0.28 eV of bulk PbSe crystals [91].

The XRD pattern of Sn+Se mixture milled for 30 min (Fig. 10) confirmed the presence of orthorhombic SnSe phase (JCPDS PDF 32-1382). TEM analysis determined that SnSe crystals exhibit a wide size range from 5 up to 500 nm. The large crystals have an indistinct shape, whereas smaller SnSe nanocrystals show a plate-like morphology. The

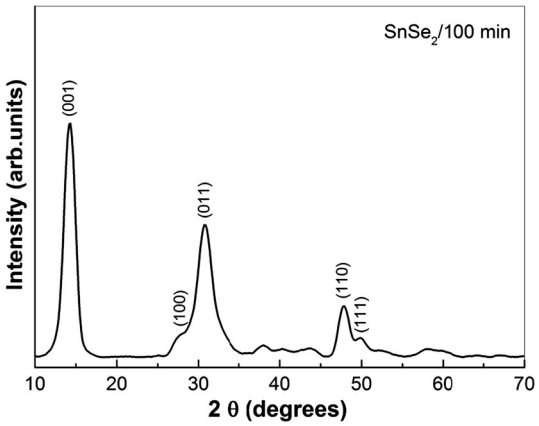

Figure 12 XRD patterns of $SnSe_2$, mechanochemically synthesized for 100 min.

nanosized SnSe crystals are shown in Fig. 11b. The presence of nanocrystalline SnO_2 (JCPDS PDF 46-1088), created as a consequence of Sn reactivity with the air during milling, was also detected [83]. The optical absorption spectrum of SnSe was recorded in the spectral range of 320–3000 nm. It was found through extrapolation of linear dependencies of $(\alpha hv)^{1/2}$ versus hv to $\alpha hv = 0$ that indirect band gap energy, $E_{g,ind}$ is equal to 0.4 eV. The indirect character of the band gap is typical for orthorhombic IV–VI compounds. For identification of the presence of higher-energy electronic transitions from the valence to conduction band, the optical absorption data were interpolated to the semiconductor absorption function corresponding to the direct band-to-band transitions. Such direct transition band gaps have higher value than indirect transitions. Based on a plot $(\alpha hv)^2$ versus hv, the value of 0.9 eV was found for direct band gap energy, $E_{g,dir}$. From our results

$$\Delta E = E_{g,dir} - E_{g,ind} = 0.5 \text{ eV} \quad (5)$$

which is in good accordance with the value 0.4 eV reported in Ref. [92]. This finding revealed the band gaps with slightly lower values, which are probably related to the disordered structure of mechanochemically prepared SnSe nanocrystals [83, 93].

$SnSe_2$ Tin diselenide $SnSe_2$ was synthesized by milling for 100 min [94]. The peaks in the XRD pattern in Fig. 12 correspond to the hexagonal $SnSe_2$ phase (JCPDS PDF 89-3197). The ^{119}Sn MAS NMR spectroscopy of mechanochemically synthesized $SnSe_2$ revealed also small amounts of tin oxides phases, analogous to tin monoselenide, SnSe, synthesized earlier [93]. According to TEM study

(Fig. 13), the morphology of $SnSe_2$ nanocrystals is bipyramidal-hexagonal with the space group P3-m1 and particle size ranging from a few to more than 100 nm [83, 94]. From UV–Vis–NIR optical absorption spectrum of mechanochemically synthesized $SnSe_2$, an indirect allowed optical transition with energy band gap of 1.0 eV was assigned, which is in accordance with band gap values for bulk single crystals of $SnSe_2$ [95–97]. The band gap value of 1.25 eV received from the intercept of the extrapolated higher-energy linear region with the hv axis—plot of $(\alpha hv)^2$ versus hv—corresponds to the direct allowed optical transition. El-Nahass has presented the direct allowed energy gap values from 1.97 to 2.1 eV for the crystalline and amorphous $SnSe_2$ [98]. Hence, the mechanochemically synthesized $SnSe_2$ semiconductor has demonstrated different types of transitions in the lattice. The electrochemical properties of such $SnSe_2$ were also tested because of its use as electrode material for lithium cells. However, the specific capacity of lithium cells with $SnSe_2$ material rapidly dropped from initial capacity 991 $mAh.g^{-1}$ to 40 $mAh.g^{-1}$ after 100 cycles. This is due to the irreversible formation of Li_xSe and metallic Sn during galvanostatic cycling of lithium cells [83].

BiSe The nanocrystalline BiSe was prepared by mechanochemical reaction which was completed after 10 min of milling. The XRD peaks in Fig. 14 were identified on JCPDS PDF card 29-246 and correspond to the hexagonal BiSe (nevskite). The BiSe has an anisotropic layered structure, and TEM analysis has revealed the microstructural appearance of BiSe with larger grains (up to 200 nm) creating the agglomerates and nanosized grains (about 5 nm) (Fig. 15). Atomic ratio Bi:Se = 1:1 was confirmed by energy-dispersive spectroscopy (EDS). The optical band gap energy of 1.06 eV was obtained from the recorded UV–Vis absorption spectrum, which was mathematically processed according to the Fermi's golden rule for direct allowed electronic transitions from the valence to the conduction band [83, 99].

Bi_2Se_3 The Bi_2Se_3 direct semiconductor was prepared by a mechanochemical synthesis in 10 min. The XRD peaks in Fig. 14 are consistent with hexagonal paraguanajuatite phase (JCPDS PDF 33-214). Bi_2Se_3 has a closely related atomic structure with BiSe. Its strongly anisotropic layered structure is due to the van der Waals gap between the pairs of Se–Bi–Se–Bi–Se atoms sheets blocks at the Se–Se contacts. The results of TEM analysis of Bi_2Se_3 were very

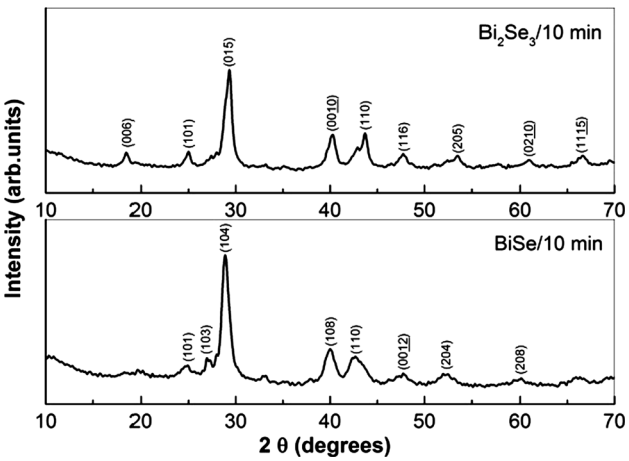

Figure 14 XRD patterns of BiSe and Bi_2Se_3, mechanochemically synthesized for 10 min.

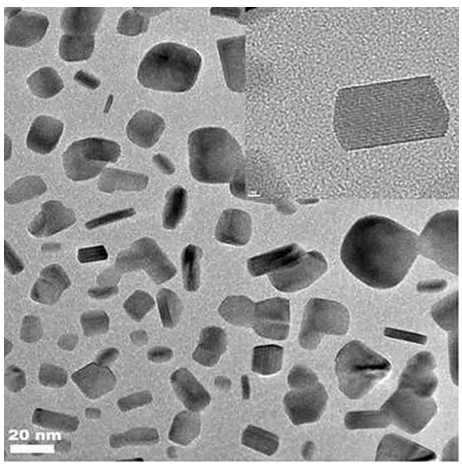

Figure 13 TEM image of nanocrystalline $SnSe_2$ with a detail of one single crystal.

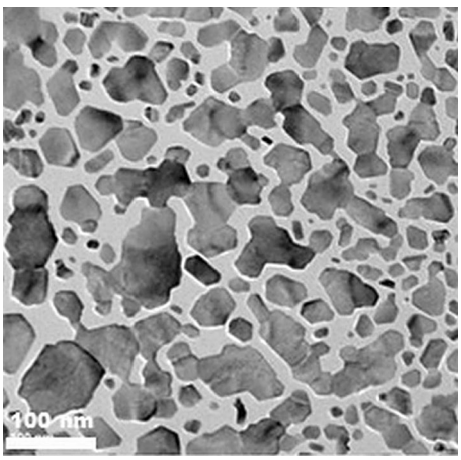

Figure 15 TEM image of nanocrystalline BiSe.

similar to that of BiSe (Fig. 16). The chemical composition of Bi_2Se_3 was confirmed also by EDS, as the atomic ratio Bi:Se = 2:3 was revealed. The higher band gap value of direct semiconductor Bi_2Se_3 (1.37 eV) in comparison with its bulk value 0.35 eV indicates a blueshift phenomenon due to the quantum size effect. This effect can be attributed to the existence of very small Bi_2Se_3 nanoparticles agglomerated into big clusters [83, 99]. The mechanochemically synthesized Bi_2Se_3 was also tested as an electrode material in lithium cells. Its initial discharge capacity 91 mAh.g^{-1} dropped of about 12% after 5 cycles. The values stabilized above 60 mAh.g^{-1} and slowly decreased towards a value of about 35 mAh.g^{-1} after 100 cycles [83].

CoSe The mechanochemical synthesis of hexagonal CoSe (freboldite, JCPDS PDF 77-7572) with a nickeline-type structure was completed after 120 min of milling, which was confirmed by XRD analysis (Fig. 17). TEM analysis of CoSe showed randomly oriented nanocrystalline particles with diameter from 5 to 25 nm, which are firmly bonded into clusters with diameter of 100 nm and more (Fig. 18). By UV–Vis measurements, the band gap energy of 1.70 eV was determined, which indicates direct optical transition in CoSe semiconductor. The obtained value of the band gap energy is blueshifted relatively to the value 1.53 eV for electrodeposited CoSe, which responds to bulk CoSe [100] and is assigned to the optical transitions of the excitonic states in the material. The obvious blueshift could be attributed to the existence of very small CoSe nanocrystalline particles agglomerated into large clusters.

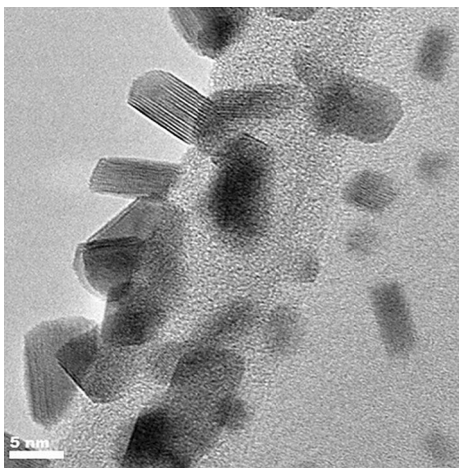

Figure 16 TEM image of nanocrystalline Bi_2Se_3 particles with the characteristic layered structure.

Recently, Al- and Ga-based selenides (Al_2Se_3, Ga_2Se_3 together with the appropriate sulphides), being promising photoelectronic materials, have been synthesized [101–103]. Moreover, further interesting selenides based on iron and applicable as superconductors were also synthesized [104–107]. All these metal selenides were successfully prepared by a simple, fast and less-consumptive mechanochemical route in laboratory mills. Very recently, a new work appeared on cobalt selenide mechanochemical synthesis by two co-authors of this review paper [108].

Tellurides Besides sulphides and selenides, also tellurides have been prepared by a mechanochemical synthesis in the previous decade [109, 110]. The new insight into the mechanism of Bi_2Te_3 synthesis has been documented in [111]. In the cited paper, an evidence of a third type of mechanochemical

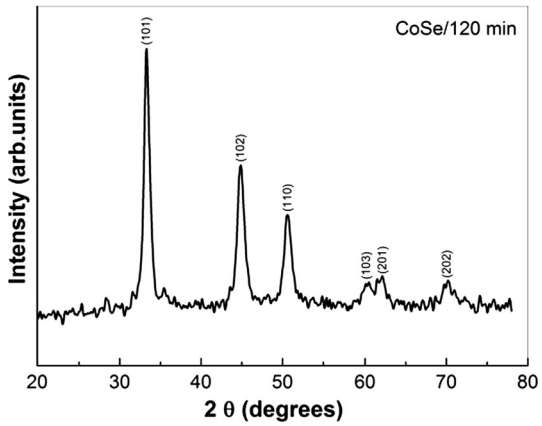

Figure 17 XRD pattern of CoSe, mechanochemically synthesized for 120 min.

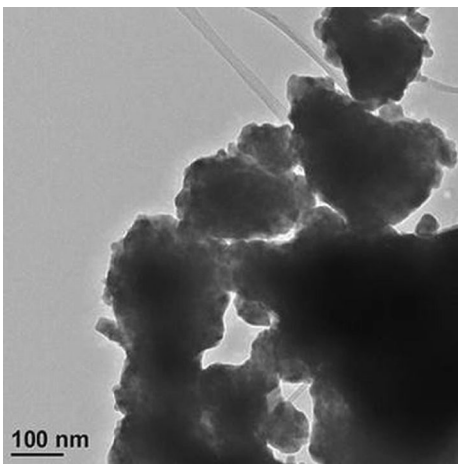

Figure 18 TEM image of nanocrystalline CoSe particles.

synthesis besides the gradual and self-propagating ones was documented. For this system, a melt-driven mechanochemical reaction was elucidated. A systematic effort to mechanochemically synthesize Cd, Zn and Ni tellurides has been manifested by Campos et al. [112–114].

Synthesis from compounds

Besides elements, also compounds can be used as precursors for the synthesis of chalcogenides. Mechanochemically synthesized nanocrystalline sulphides from corresponding metal acetates and sulphur precursors were prepared by high-energy milling according to the reaction:

$$(CH_3COO)_2Me \cdot xH_2O + Na_2S \cdot 9H_2O \rightarrow MeS + 2CH_3COONa + (x+9)H_2O \quad (6)$$

The above-mentioned acetate route has been applied for the synthesis of Zn, Cd and Pb nanocrystalline sulphide semiconductors on laboratory [28] and industrial scale [115].

ZnS ZnS nanoparticles were prepared by high-energy milling of zinc acetate and sodium sulphide according to the above-described reaction. After the completion of reaction, the synthesized ZnS nanoparticles have been washed, decanted and dried, according to the procedure described in [28]. The properties of mechanochemically synthesized ZnS were compared with the chemically precipitated ZnS in [33]. The XRD pattern of the mechanochemically synthesized ZnS (Fig. 19a) shows mainly the reflections of cubic phase, which is also supported by relative intensity. The higher background on the XRD pattern implies the formation of some amorphous material.

HRTEM technique allows the determination of size of the nanoparticles, the type of structures produced and also the possible induced morphologies (Fig. 19Ba–d). In Fig. 19B-a, the area of 16 nm × 16 nm, where several clusters are clearly identified, is shown. Particularly, three of those clusters with sizes of 2.6, 3.7 and 3.4 nm can be observed. In fact, the corresponding fast Fourier transformation technique image denotes a polycrystalline material, which must be composed by the nanocrystals. Higher magnification allows determining the lattice distance of the material, as shown in Fig. 19B-b. A square contrast in the centre of the micrograph with interplanar distances of 0.27 and 0.28 nm, that implies a region with an axis zone near to the (001), was found. Figure 19B-c shows a well-defined cluster of ~4 nm in size with a hexagonal profile and rhombic internal contrast, that is characteristic of a truncated octahedron particle observed in the (011) zone axis. The HRTEM images allow finding defects in the nanocrystalline material, as marked with an arrow in Fig. 19B-d [33].

CdS The structural and surface properties of the mechanochemically synthesized nanocrystalline CdS

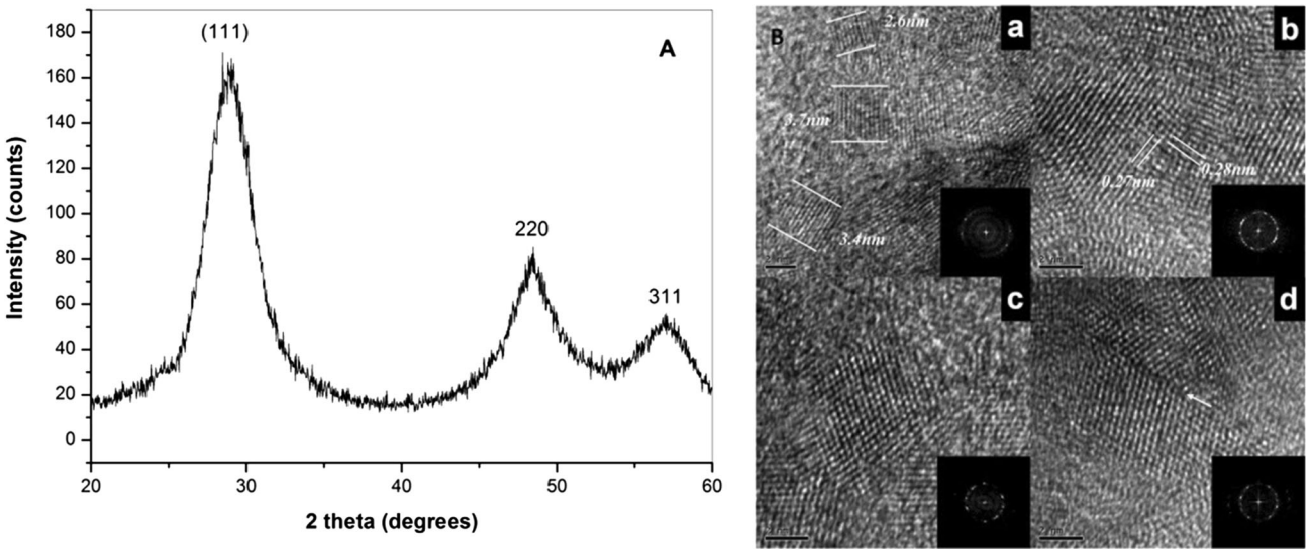

Figure 19 Characterization of mechanochemically synthesized ZnS: **A** XRD pattern and **B** HRTEM micrographs (*a*) identification of nanoparticle with size around 3 nm, *b* determination of structure with the help of the interplanar distance measurement, *c* hexagonal profiles for fcc-like nanoparticles, *d* example of fracture induced in the nanoparticles [33].

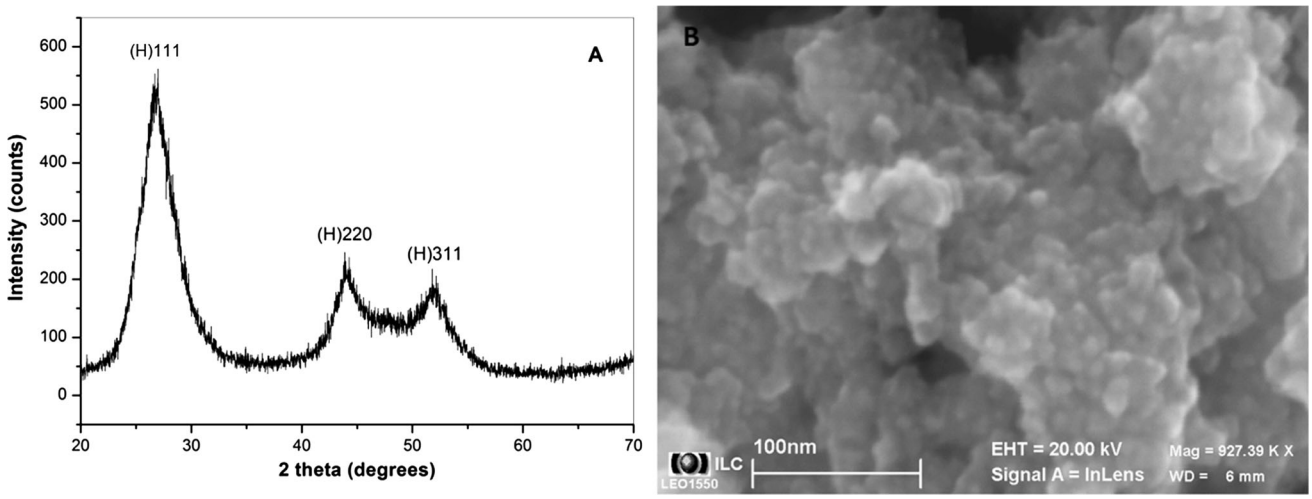

Figure 20 **a** XRD pattern and **b** SEM of mechanochemically synthesized CdS. Reprinted with permission from Ref. [40]. Copyright 2009, Springer.

particles in the planetary mill were studied in paper [40]. The cubic structure with the peaks associated with (111) (220) and (311) planes was clearly identified (Fig. 20a). CdS nanocrystallites with particle size 2 nm exhibit quantum size effect. The mechanochemically synthesized CdS nanoparticles, in comparison with chemically synthesized CdS, are distinguished by their physicochemical properties. The advantage of mechanochemical synthesis in the production of CdS nanoparticles over the chemical route is in the production of particles with large surface area, as well as in the formation of uniform crystallites.

Surface morphology of the synthesized CdS nanoparticles with estimated size from 20 to 30 nm is shown in the SEM image in Fig. 20b. Individual nanoparticles have a tendency to form nanoparticle agglomerates during milling process, and both entities can be clearly seen in the image.

PbS PbS nanocrystals have been successfully prepared using a surfactant-assisted mechanochemical synthesis [32, 38]. The XRD patterns confirmed the presence of galena PbS (JCPDS 5-592), whatever treatment conditions were applied (Fig. 21). The intensive peaks in XRD patterns indicate highly crystalline nature of PbS nanostructures. The crystallite sizes calculated from XRD data using Warren–Averbach method and further confirmed by high-resolution SEM images were 3, 8, 11 and 19 nm for surfactant-free and three different surfactant-assisted mechanochemical syntheses, respectively. The surfactants facilitate the preferential growth of PbS nanocrystals in (200) direction [38].

Recently, Tolia et al. [116] published a paper on mechanochemical synthesis and characterization of group II–VI semiconductor nanoparticles, namely ZnS, CdS, PbS and CuS. The synthesis was carried out in a high-energy ball mill from corresponding metal acetate and sodium sulphide. The same mill and precursors were applied also in papers [28, 32, 33, 38, 40]. In comparison with these papers, very long milling time (10 h) was used in paper [116], most probably because of lower applied rotation speed (350 rpm). On the other hand, very thorough examination of the prepared nanocrystalline products (concretely via XRD, TEM and UV–Vis methods) was performed therein.

Bio-inspired synthesis

Nature has fascinated people for a very long time, and some researchers realized that it provides very useful tools for the synthesis of specific materials. The synthetic process using natural materials is called "bio-inspired synthesis" [117]. Based on the scale of bio-inspired candidates, bio-inspired syntheses can be divided into two different types, namely synthesis using (1) biomatrices with sizes ranging from nanometres and microns to macroscale and (2) water-soluble DNA, proteins or those biomolecules secreted or extracted from microorganisms and plants [118]. However, in the majority of cases, this approach is

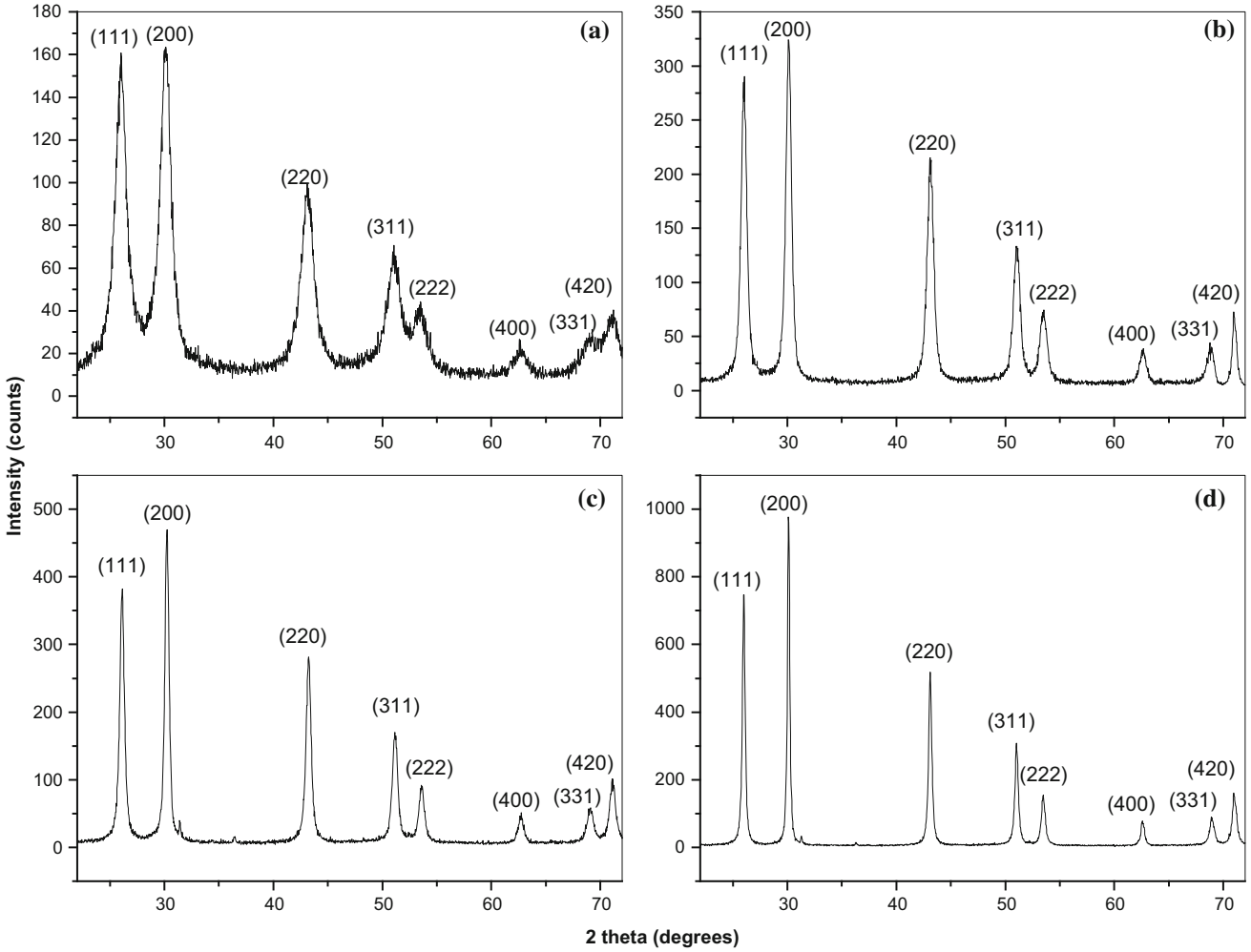

Figure 21 XRD patterns of mechanochemically synthesized PbS: **a** no surfactant, **b** ethylenediamine (EDA), **c** sodium dodecyl sulphate (SDS), **d** ethylenediaminetetraacetic disodium salt dihydrate (EDH). Reprinted with permission from Ref. [38], Copyright 2011, Elsevier.

used to synthesize metallic nanoparticles in their elemental forms. The field of bio-inspired synthesis of binary or more complicated compounds is also expanding, but as can be traced in the recent literature, not so quickly. As examples, a few papers on the bio-inspired synthesis of chalcogenides [119], or more concretely sulphides [120–124] and tellurides [125] can be mentioned.

PbS The combination of bio-inspired synthesis and mechanochemistry is quite exotic, as the soft natural materials are expected to lose their unique properties when subjected to high-energy milling. Nevertheless, it can be beneficial in some cases, as due to milling, some reactive sites can be exposed and interact with surrounding species. Our research group has successfully proved that it is possible to utilize ball milling of natural materials to synthesize binary compound, concretely lead sulphide [35, 126] which is a semiconductor material and can be used in various fields.

In the first paper [126], the eggshell membrane, known to have multidisciplinary applications [127] and has been already used as a bio-template for PbS and PbSe [128], was utilized as a source of sulphur. As a source of lead, lead acetate was applied, thus following the acetate route of the sulphides synthesis [28]. The two precursors were co-milled for 180 min, and the XRD pattern and SEM image of the product were recorded (Fig. 22).

The successful synthesis of lead sulphide was confirmed by matching the obtained reflections of crystallographic planes in the XRD pattern with the JCPDS database data for PbS (Fig. 22a). The embedment into the residual matrix of the ESM can be seen

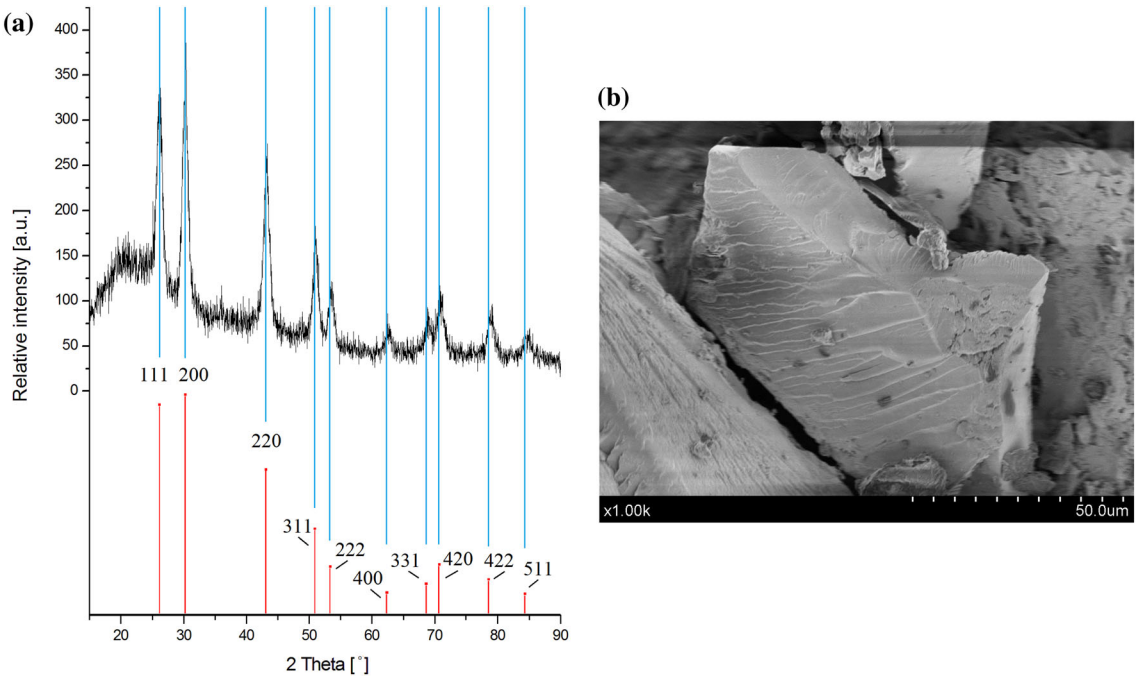

Figure 22 Mechanochemically synthesized PbS using eggshell membrane: **a** XRD pattern—*blue lines* correspond to the reflections of the planes of crystalline PbS; **b** SEM image of the particle obtained after 180 min of milling. Reprinted with permission from Ref. [126]. Copyright 2013, Elsevier.

in the SEM micrograph (Fig. 22b). The separation of the NPs from the resulting matrix is still a challenge.

In another paper [35], it was proven that cysteine, an essential amino acid present in the eggshell membrane [129], is the compound releasing sulphur from its structure to interact with lead. Instead of cysteine, its dimer cystine was used, as it was hypothesized that upon milling, the disulphide bridge could be broken and sulphur could be released for the reaction. It was co-milled, again, with lead acetate. The progress of the mechanochemical reaction was monitored by XRD (Fig. 23a), and the morphology of the prepared nanoparticles was monitored by TEM (Fig. 23b).

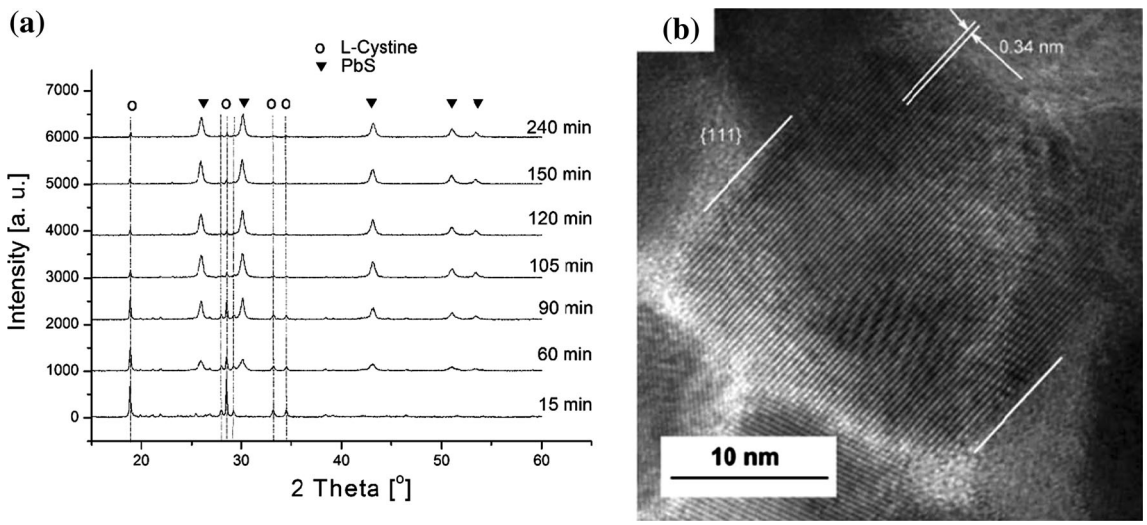

Figure 23 Mechanochemically synthesized PbS using L-cystine: **a** XRD pattern; **b** HRTEM image of the particle obtained after 105 min of milling. Reprinted with permission from Ref. [35]. Copyright 2014, Royal Society of Chemistry.

The intensity of the peaks of cystine has gradually decreased, and the intensity of the peaks of the product increased until 105 min. Further milling did not bring about any changes, so 105 min was considered the final reaction time. The HRTEM image (Fig. 23b) shows a nanocrystal with the interplanar distances of 0.34 nm, which correspond to (111) planes distances of PbS. Moreover, it suggested that PbS nanoparticles are wrapped by L-cystine (light regions in Fig. 23b). From these results, it was concluded that cystine plays a dual role in our system, as it successfully serves as a source of sulphur and is deposited on the surface of the prepared sulphide on the other hand.

These two reports represent a nice example how mechanochemistry can be utilized in the field of bio-inspired synthesis of binary compounds. This particular field of research is expected to expand in future.

Ternary chalcogenides

Synthesis from elements

Ternary chalcogenide semiconductors of the I–III–VI_2 group have received considerable attention over the last decades due to their photoconductivity characteristics and other beneficial intrinsic properties, which make them suitable candidates for photoelectrochemical cells [130]. Among different materials, $CuInSe_2$, $CuInS_2$ and Cu_2SnS_3 are effective light-absorbing materials, which can be used in thin-film solar cells or in printable and flexible photovoltaic devices. These materials possess advantageous properties for solar applications, since their band gap energy is at the red edge of the visible solar spectrum (bulk $CuInSe_2$ and $CuInS_2$ have band gap energies of 1.05 and 1.5 eV, respectively) [131]. Moreover, also chalcopyrite, $CuFeS_2$ represents earth-abundant thermoelectric material [132].

$CuInS_2$ Ternary $CuInS_2$ nanoparticles were mechanochemically prepared from copper, indium and sulphur elements [133] according to the reaction:

$$Cu + In + 2S \rightarrow CuInS_2 \quad (7)$$

The mechanochemical synthesis of $CuInS_2$ was finished after 60 min, as it is illustrated by the corresponding XRD pattern (Fig. 24a). The product was identified as roquesite, $CuInS_2$ (JCPDS 027-0159). The crystal structure has a tetragonal body-centred symmetry belonging to the I-42d space group with the lattice parameters $a = b = 5.523$ Å and $c = 11.141$ Å. The characteristic peaks of other impurities were not detected. The most intense peak at 27.9° is attributed to the $CuInS_2$ phase with chalcopyrite structure oriented along the [112] crystal plane. The estimated average crystallite size is 18 nm for the $CuInS_2$ [133].

Raman spectroscopy confirmed pure crystalline nanoparticle formation. In Fig. 24b, the micro-Raman spectra of the synthesized sample are provided. The dominant features of Raman plots are intense peaks at 298 cm^{-1} and the weaker peaks at 240 and 340 cm^{-1}, which were previously assigned to the A1, E and B2 modes of $CuInS_2$ phase, respectively [134]. No other Raman peaks were observed, indicating pure $CuInS_2$ nanoparticles. It can be also seen that at

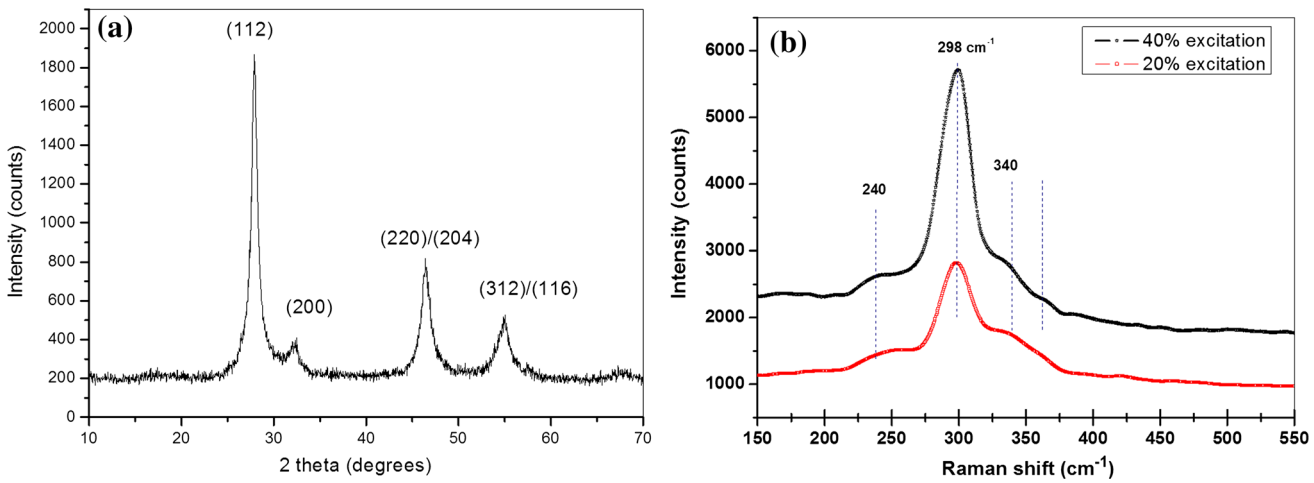

Figure 24 **a** XRD pattern and **b** micro-Raman spectrum of the $CuInS_2$ nanoparticles synthesized during 60 min of milling. Reprinted with permission from Ref. [133]. Copyright 2016, Springer.

40% excitation power, the recrystallization of the structure occurs, which is manifested by increasing and narrowing of the peak at 298 cm^{-1} and decreasing of the intensity of other peaks in comparison with the Raman spectra measured at only 20% excitation power by laser light [133].

The microstructure of the $CuInS_2$ sample after 60 min of milling was further studied using TEM and HRTEM, and the obtained results are depicted in Fig. 25. In the TEM image (Fig. 25a), it can be seen that the sample is formed by quite large particles (100–300 nm). This result is in a good agreement with that determined by photon cross-correlation spectroscopy (not shown here). However, the HRTEM images show that those particles are formed by agglomerated nanocrystals of $CuInS_2$ with very small crystallite size (10–20 nm), confirming the results of XRD analysis. At edges of some particles, the initial crystallization and some amorphous areas can be observed (Fig. 25b). Some oriented nanocrystals were elucidated from the contrast (marked with a white square) in the images presented in Fig. 25c and d, and the fast Fourier transform (FFT) was done to estimate the zone axis of the orientation. The results show the [110], [201] and [531] zone axes of the tetragonal roquesite system.

In paper [135], $CuInS_2$ powders were synthesized by mechanochemical process from elementary precursors. A self-propagating combustion occurred during milling. Once the reaction (6) is ignited, the combustion propagates quickly and the whole process could only last for several seconds. The authors also studied the morphology evolution of Cu–In–S mixture before combustion reaction, and based on the results, they figured out the following sequence of processes: (1) starting powders are mixed, flattened or fragmented, (2) particle layers are formed, (3) agglomerated particles are formed, and (4) with progress of the mechanochemical reaction, the reactants are mixed on an atomic scale.

Also cryogenic milling has been applied for mechanochemical synthesis of $CuInS_2$. This approach improves the results in terms of the product size and processing times. The agglomeration is prevented in this case. Liquid nitrogen as a medium in milling and the powders of Cu_2S and In_2S_3 as precursors with respect to the stoichiometry of $CuInS_2$ were used [136].

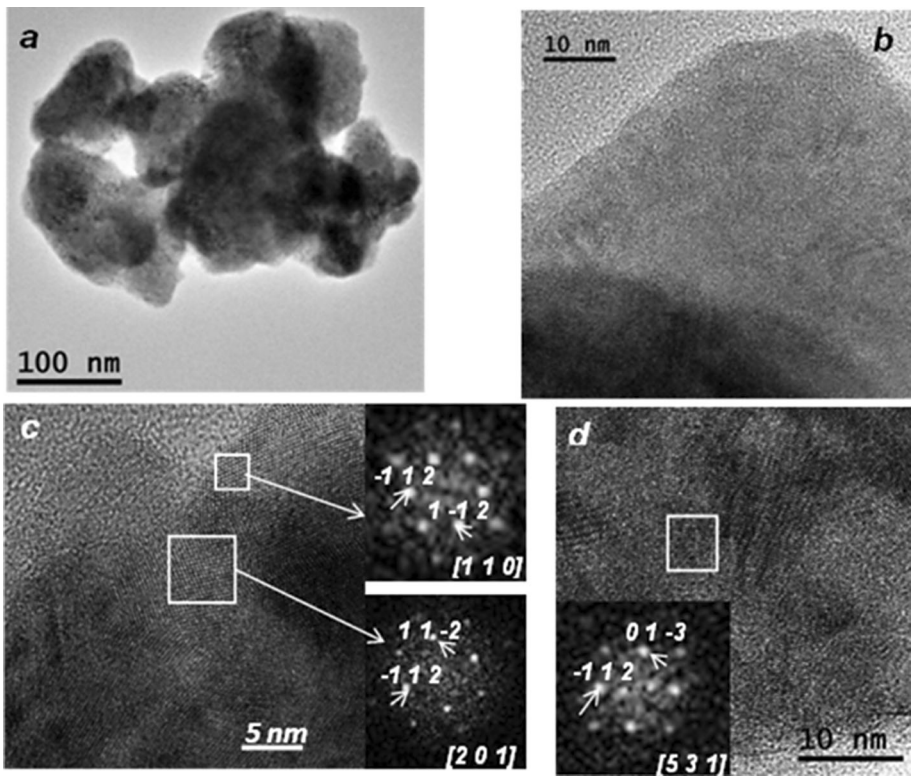

Figure 25 Microcharacterization of $CuInS_2$ sample synthesized mechanochemically for 60 min: (**a**) TEM image; (**b**–**d**) HRTEM micrographs. Reprinted with permission from Ref. [133]. Copyright 2016, Springer.

$CuFeS_2$ Chalcopyrite, $CuFeS_2$, is the most abundant copper mineral used for metal recovery in extractive metallurgy [1, 27]. However, it has been also identified as a suitable candidate for environmentally friendly thermoelectric materials recently. In the paper [137], chalcopyrite was synthesized from elemental powders of Cu, Fe and S. The progress of the synthesis was monitored by using the XRD (Fig. 26). The reaction to $CuFeS_2$ proceeds via the formation of the CuS at the beginning. With increasing milling time, also Fe is consumed and finally chalcopyrite is formed. According to this study, the electrical conductivity of sulphur-deficient $CuFeS_{2-x}$ increases with decreasing S content, whereas its thermal conductivity is decreasing.

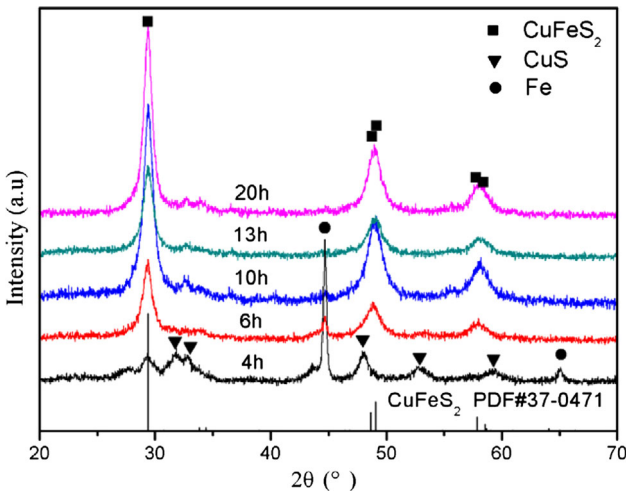

Figure 26 XRD patterns of the powders at stoichiometric composition ($CuFeS_2$) after mechanochemical synthesis for different times. Reprinted with permission from Ref. [137]. Copyright 2014, Elsevier.

Cu_2SnS_3 A p-type ternary copper-containing chalcogenide semiconductor Cu_2SnS_3 (mohite) becomes more and more interesting, because of its application in photovoltaic devices, light-emitting diodes and nonlinear optical materials [138]. In this paper, the combined procedure was applied: in the first step Cu, Sn and S powders were mixed and grinded in a mortar. In the second step, the mixture was put in a boat crucible in a tube furnace and heated at 600 °C for 2 h under argon. A black powder was obtained and further characterized. In another work, mohite was also mechanochemically synthesized from Cu, Sn and S powders for 12–60 h. For further processing, polyvinylpyrrolidone was used as an organic stabilizing agent for the preparation of a printable paste.

$CuInSe_2$ Nanocrystalline ternary $CuInSe_2$ particles have been prepared by high-energy milling in a planetary mill in argon atmosphere from copper, indium and selenium elements [139], following the reaction:

$$Cu + In + 2Se \rightarrow CuInSe_2. \quad (8)$$

The mechanochemical synthesis of $CuInSe_2$ was finished after 60 min of milling (Fig. 27a), and the product was identified as copper indium diselenide $CuInSe_2$ (JCPDS 00-040-1487). All the diffraction lines (112), (220), (312) responded well to JCPDS card of the pure tetragonal $CuInSe_2$. This structure belongs to the I-42d space group, with lattice constants

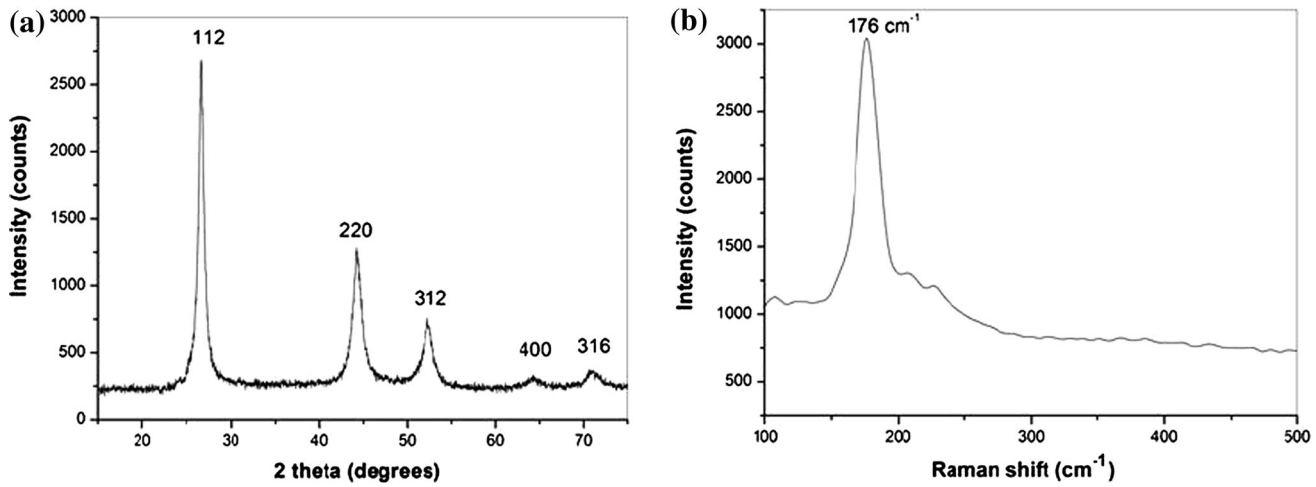

Figure 27 **a** XRD pattern and **b** micro-Raman spectrum of the $CuInSe_2$ nanoparticles synthesized during 60 min of milling. Reprinted with permission from Ref. [139]. Copyright 2016, Elsevier.

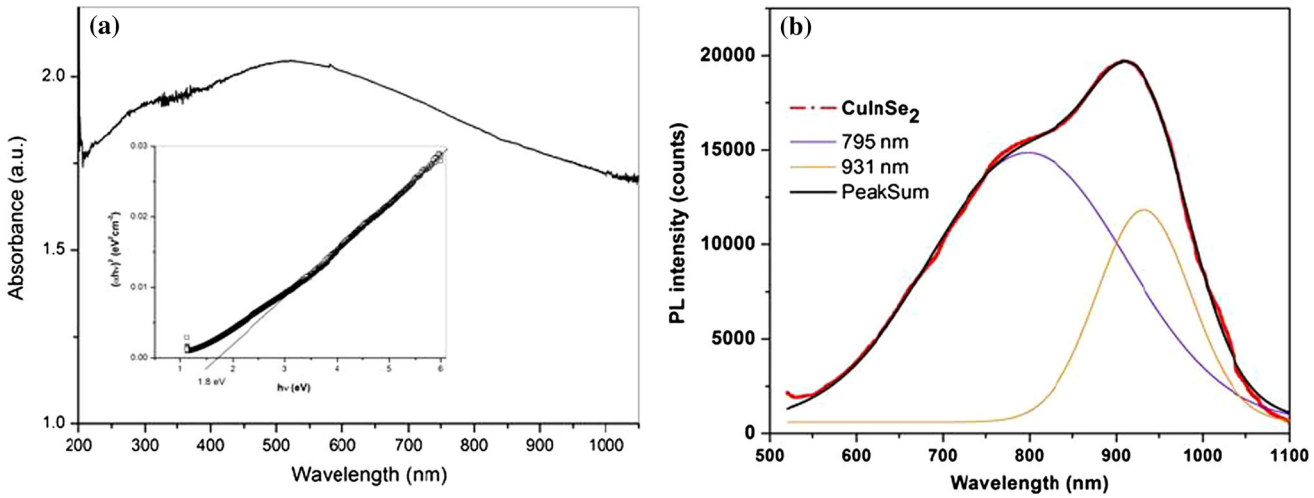

Figure 28 **a** UV–Vis absorption (variation of $(\alpha hv)^2$ vs. hv is shown in *inset*) and **b** micro-photoluminescence spectrum of the $CuInSe_2$ synthesized during 60 min of milling. Reprinted with permission from Ref. [139]. Copyright 2016, Elsevier.

$a = b = 5.782$ Å and $c = 11.619$ Å. Moreover, other phases were not detected, confirming the high purity of prepared $CuInSe_2$ sample. The average crystallite size, evaluated using the Rietveld analysis, was determined as 31 nm.

The Raman spectrum of $CuInSe_2$ nanoparticles shows a strong peak at 176 cm^{-1} corresponding to the A1 phonon mode of tetragonal $CuInSe_2$ having chalcopyrite structure (Fig. 27b). The blueshift in relation to the frequency of bulk $CuInSe_2$ A1 mode described in paper [140] is probably caused by the nanocrystalline character of the prepared $CuInSe_2$.

In Fig. 28a, the UV–Vis spectrum of $CuInSe_2$ milled during 60 min is shown. By extrapolating of $(\alpha hv)^2$ against (hv) plot to $(\alpha hv)^2 = 0$ (inset of Fig. 28a), the optical band gap was evaluated. The calculated band gap of $CuInSe_2$ nanoparticles was determined as 1.8 eV and shows a blueshift of about 0.75 eV compared to the bulk $CuInSe_2$ with band gap of 1.05 eV [141]. In addition, it follows from the linear nature of the plot that the synthesized $CuInSe_2$ nanoparticles have a direct band gap. The obtained value is consistent with the results published in paper [142]. These results showed that the shape and the size of semiconductor particles affect the absorption edge and the band gap.

The room-temperature micro-photoluminescence (PL) spectrum of the mechanochemically synthesized $CuInSe_2$ particles with the exciting wavelength at 514 nm is presented in Fig. 28b. Two peaks can be detected in the measured spectra, concretely at 795 nm (1.56 eV) and 931 nm (1.33 eV). The emission spectrum is blueshifted in relation to the band gap of bulk $CuInSe_2$ and may be attributed to band emissions from different small nanocrystalline domains or clusters. This is in coincidence with absorption measurements where a long tail of low-energy absorption is resolvable in the measured spectra. Similarly, the explanation regarding the alternative carrier recombination between the quantized conduction band minimum and defect trap level in $CuInSe_2$ nanoparticles is also persuasive.

Other ternary sulphides Recently, eco-friendly and low-cost sulphide-based materials were prepared by a combination of mechanical treatment and spark plasma sintering of corresponding elements. Compounds like $CuSbS_2$, Cu_3SbS_4 and Ge-doped Cu_3SbS_4 show intrinsically low thermal conductivity and are good candidates for thermoelectric technology, which can directly convert waste heat into useful electricity [143–145].

Synthesis from compounds

$Cd_xZn_{1-x}S$ Mechanochemical solid-state synthesis of $Cd_{0.5}Zn_{0.5}S$ nanocrystals was performed using Cd and Zn acetates and sodium sulphide as precursors [37, 41]. The synthesis proceeds according to scheme:

$$x(CH_3COO)_2Cd \cdot 2H_2O + (1-x)(CH_3COO)_2Zn \cdot 2H_2O + 2Na_2S \cdot 9H_2O \rightarrow Cd_xZn_{1-x}S + 4CH_3COONa + 13H_2O \quad (9)$$

where $x = 1$, 0.5 and 0, respectively. Figure 29 shows the powder XRD patterns. As a result of high-energy

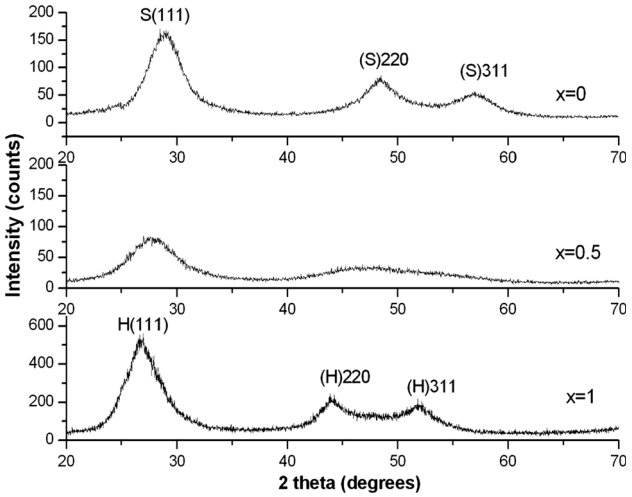

Figure 29 XRD patterns of mechanochemically synthesized $Cd_xZn_{1-x}S$. Reprinted with permission from Ref. [41]. Copyright 2008, Elsevier.

milling, the produced particles are composed of small crystallites with crystalline size ~2 nm. The crystallites are formed by cubic phase sphalerite (S), ZnS and hawleyite (H), CdS. As for $Cd_{0.5}Zn_{0.5}S$ nanoparticles, the diffraction peaks gradually shifted to larger angles and a phase transition H → S with an increase of zinc content was observed during milling. This shifting also indicates that there is no phase separation or separated nucleation of CdS and ZnS in $Cd_{0.5}Zn_{0.5}S$ nanocrystals.

Quaternary chalcogenides

There is a general paradox in present research and application of quaternary chalcogenide solar materials. On one hand, CIGS (copper indium gallium selenide) solar cells attracted a big attention owing to their high power conversion efficiency and good stability. On the other hand, these materials represent the potential environmental problem because of Se toxicity and are economically unfavourable because of limited availability and high price of In and Ga [146–149]. The solution can be a substitution of individual elements in CIGS. For example, stannite, Cu_2FeSnS_4 (CFTS), and kesterite, Cu_2ZnSnS_4 (CZTS), provide promising alternatives to conventional photovoltaic materials. They have suitable band gap, high absorption coefficient and high radiation stability [148, 150, 151]. The elemental components are environmentally acceptable (application of S instead of toxic Se), cheap and available (application of earth-abundant Fe, Zn and Sn instead of scarce In and Ga).

Synthesis from elements and compounds

Kesterite represents a hot candidate for the application in the area of photovoltaic materials. Its absorption coefficient of 10^4 cm^{-1} and the ideal band gap of 1.5 eV classify it as one of the ideal p-type semiconductors available to thin-film solar cell absorbers [152]. Moreover, the band gap tuning is possible by the modification of kesterite chemical composition and by its thermal and mechanical treatment. However, until now, the best achieved efficiency for CZTS is only 12.6% [153]. This is far away from the best Si, CIGS and CdTe solar cells that have efficiencies of 25.6, 21.7 and 21.5%, respectively [154, 155]. Therefore, there is still a lot of room for the improvement of this characteristics, which opens up possibilities for further research. A large variety of routes for kesterite synthesis have been undertaken so far. These routes include various vacuum deposition techniques, such as sputtering, co-evaporation, pulsed laser deposition and non-vacuum-based syntheses such as electrodeposition and solution-based approaches. These synthetic pathways were reviewed in [156] (see also the citations therein). Solution-based approaches include solvothermal processes, hot injection and microwave irradiation [157] (see also the citations therein). Many other methods are being applied, as summarized in [158].

However, solid-state synthesis methods for CZTS preparation are becoming more and more popular. Their environmental acceptance as a green process, cost-effectiveness and effectivity of mechanochemical synthesis attract researches permanently in recent years. CZTS has been successfully synthesized from elements [157–164], as well as from compounds [165–170]. The formal equation for kesterite Cu_2ZnSnS_4 synthesis from elements is:

$$2Cu + Zn + Sn + 4S \rightarrow Cu_2ZnSnS_4 \quad (10)$$

The knowledge permanently gained from mechanochemical synthesis of binary and ternary compounds served as know-how for the synthesis of quaternary compounds. Very effective planetary mills [9], preferentially working with ZrO_2 and steel media, were applied. In dependence on milling parameters like ball-to-powder ratio or revolution speed, various milling times were applied. In some cases, butanol has been applied during milling with the intention to obtain a good homogenization and produce a good material for film preparation [154, 164]. A simplified

scheme of kesterite Cu_2ZnSnS_4 synthesis from elements is shown in Fig. 30.

However, the mechanism of synthesis is not as simple as given by Eq. (10). Pareek et al. [154], based on XRD and Raman data, published a more realistic pathway:

$$2Cu + Zn + Sn + 4S \rightarrow Cu_2S + SnS_2 + ZnS \rightarrow Cu_2SnS_3 + ZnS \rightarrow Cu_2ZnSnS_4 \quad (11)$$

The authors emphasized that the higher temperature (550 °C) favours the backward reaction:

$$Cu_2S + SnS_2 + ZnS \leftrightarrow Cu_2ZnSnS_4 \quad (12)$$

This is important by annealing of samples. Moreover, when samples bear the mechanochemical "memory", the decomposition temperature decreases, which, in the case of sulphides, can be from 100 to 200 °C lower than in the non-treated samples [1, 27].

Chalcogenide composites

Nanocomposites represent a new generation of materials where at least the size of one of the components is in the nanometre range. They found applications in various fields, among other also in bioimaging science and technology. In such a case, at least one component must have good optical properties and cannot be toxic for living organisms. Among various chalcogenides, ZnS seems to be a potential candidate for the formation of nanocomposites [171], as ZnS-based nanocomposites are finding applications in diverse fields of materials, e.g. diluted magnetic semiconductors, fluorescent probes, photocatalysis, targeted drug delivery and imaging of cancer cells [171].

Several nanocomposites obtained by mechanochemical synthesis will be described below.

CdSe/ZnS CdSe and CdS nanocrystals represent attractive materials, which are useful alternatives to fluorescent dyes. The reason for this application is their bright fluorescence, narrow emission, broad UV excitation, high photostability and biocompatibility [172]. However, Cd toxicity has to be overcome, especially when applied into living organisms. In the paper [30], the novel mechanochemical synthesis of CdSe/ZnS nanocomposite has been developed (Fig. 31). The crystallite size of this type of nanocomposite was 20–30 nm for cubic CdSe and 3–8 nm for hexagonal ZnS.

CdS/ZnS Analogous approach has been applied in [29] for the synthesis of CdS/ZnS nanocomposite. However, in this case, the "acetate route" (Fig. 1b), using Cd and Zn compounds as metal precursors, has been applied. The whole procedure including two milling steps and subsequent processing is schematically shown in Fig. 32. In this case, the crystallite size of both phases in the nanocomposite was in 3–4 nm range.

InAs/ZnS The preparation of InAs/ZnS composite was performed as a two-step process [173]. In the first step, InAs was prepared by co-milling of elemental indium and arsenic [174]. In the second step, InAs was further co-milled with the precursors for ZnS synthesis ($(CH_3COO)_2Zn.2H_2O$ and $Na_2S.9H_2O$). The milling was performed in a planetary ball mill for 20 min in the argon atmosphere. After the reaction, the obtained mixture was thoroughly washed with distilled water to remove residual sodium acetate and subsequently, after drying, a solid-phase sample of InAs/ZnS was obtained.

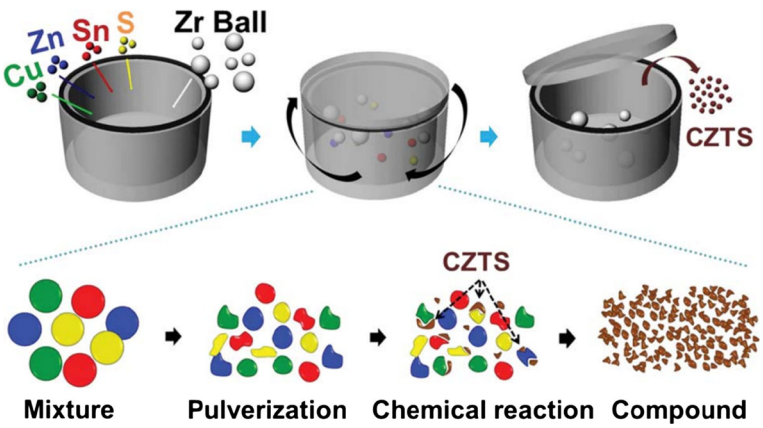

Figure 30 A schematic illustration of the synthetic procedure for CZTS nanocrystals by a mechanochemical process. Reprinted with permission from Ref. [159]. Copyright 2014, Royal Society of Chemistry.

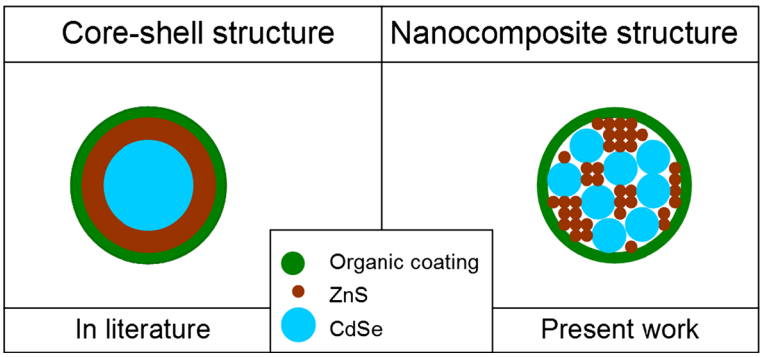

Figure 31 Schematical view of CdSe/ZnS nanocomposites (phase heterogeneity is shown) bioconjugated with organics. Reprinted with permission from Ref. [30]. Copyright 2014, Elsevier.

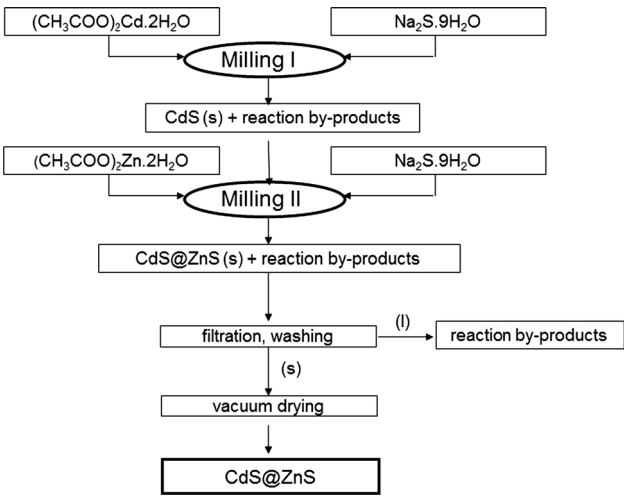

Figure 32 Mechanochemical synthesis of CdS/ZnS nanocmposites. Reprinted with permission from Ref. [29]. Copyright 2016, Elsevier.

The chemical reactions of the mentioned processes can be described as follows:

$$\mathrm{In} + \mathrm{As} \rightarrow \mathrm{InAs} \tag{13}$$

$$\mathrm{InAs} + (\mathrm{CH_3COO})_2\mathrm{Zn} \cdot 2\mathrm{H_2O} + \mathrm{Na_2S} \cdot 9\mathrm{H_2O} \rightarrow \mathrm{InAs/ZnS} + 2\mathrm{CH_3COONa} + 11\mathrm{H_2O} \tag{14}$$

The existence of InAs/ZnS binary composite was confirmed using X-ray diffraction analysis and micro-Raman spectroscopy. The broad diffraction peaks indicated that the prepared material was of very fine crystalline structure. It was estimated that the InAs component had average crystallite size of $d = 45 \pm 15$ nm, and for the ZnS, $d = 2 \pm 1$ nm was estimated. Moreover, the existence of ZnS in two crystallographic modifications, namely cubic (sphalerite), as a major phase, and hexagonal (wurtzite), was determined. The micro-Raman spectra also confirmed the presence of both phases.

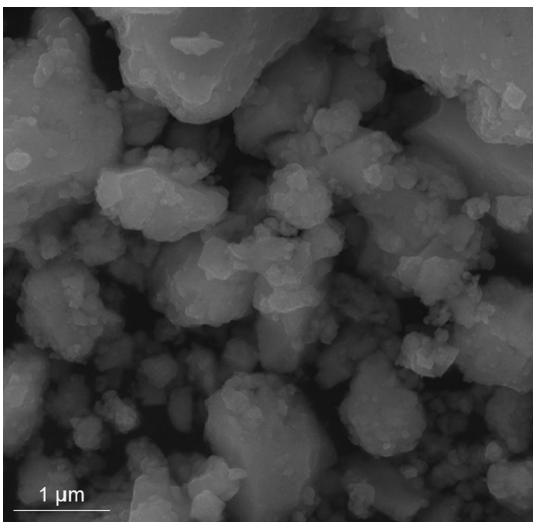

Figure 33 SEM photograph of InAs/ZnS composite.

The morphology of the prepared sample was studied using scanning electron microscopy (SEM). The results showed that the sample was formed more or less from two particle size fraction types—bigger and smaller particles with irregular shape (Fig. 33). Using energy-dispersive X-ray (EDX) mapping, it was determined that bigger ones can be attributed to InAs and smaller ones to the ZnS particles. It was concluded that the mixture is composed of two individual phases.

As_4S_4/ZnS As_4S_4/ZnS nanocomposites were prepared by milling in a planetary ball mill in argon atmosphere for 20 min [175]. The reaction proceeded in one step, according to the equation:

$$\mathrm{As_4S_4} + (\mathrm{CH_3COO})_2\mathrm{Zn} \cdot 2\mathrm{H_2O} + \mathrm{Na_2S} \cdot 9\mathrm{H_2O} \rightarrow \mathrm{As_4S_4/ZnS} + 2\mathrm{CH_3COONa} + 11\mathrm{H_2O} \tag{15}$$

As_4S_4 was used as a commercial chemical and, similarly as in the binary InAs/ZnS composite,

$(CH_3COO)_2Zn.2H_2O$ and $Na_2S.9H_2O$ were the precursors for ZnS synthesis. The samples were prepared in different molar ratios (As_4S_4:ZnS = 5:0, 4:1, 1:1, 1:4 and 0:5).

According to the JCPDS database, the sample As_4S_4/ZnS 5:0 was identified as pure arsenic sulphide. The XRD pattern was a superposition of crystalline and very significant amorphous phases. The average crystallite size was estimated as $d = 25$ nm. On the other end of the studied systems (As_4S_4/ZnS 0:5), pure zinc sulphide was identified. In this case, much smaller crystallites were calculated using a Rietveld analysis, with $d = 3.4$ nm. In the composite samples (As_4S_4/ZnS 4:1, 1:1 and 1:4), the As_4S_4 crystallite sizes varied in the samples from 25 to 40 nm and ZnS crystallite sizes were determined in a range from 2.4 to 3.4 nm.

In the prepared systems, the surface properties were also studied. The BET method was used for the calculation of specific surface area, S_A. For the pure As_4S_4 sample (As_4S_4/ZnS 5:0), this value was very small (0.3 $m^2.g^{-1}$). The isotherm for this sample was established as of type II, which is typical for non-porous or macroporous materials. By introducing ZnS into the system, the values of S_A were considerably increased (up to 68 $m^2.g^{-1}$ for the sample As_4S_4/ZnS 1:4). The shape of the isotherms changed gradually into type IV with the increasing amount of ZnS and hysteresis loops appeared, suggesting the presence of mesopores. With the increasing amount of ZnS, also total pore volume increased and average pore diameter decreased. It was not surprising that the pure ZnS sample (As_4S_4/ZnS 0:5) had the highest value of S_A (126 $m^2.g^{-1}$) and the smallest pore size (<40 nm), suggesting the mesoporous character of the sample. The incorporation of zinc sulphide into the system seemed to be very beneficial, and the results are summarized in Table 4.

Ag_2S/Sb_2S_3 The mechanochemical synthesis of Ag_2S/Sb_2S_3 amorphous fast ion semiconductor with various ratios of both components and their properties were investigated in [176]. After approximately 10 h of ball milling, the composition $0.85Ag_2S$–$0.15Sb_2S_3$ becomes amorphous and attained conductivity, which was three times higher than that of the analogous melt-quenched glass. The paper is a contribution to science and technology of ionic conductivity of the perspective materials.

Applications

This review illustrates that mechanochemistry can be used to initiate and perform various solid-state syntheses, thus turning the high-energy mill into a mechanochemical reactor [4]. Mechanochemistry finds many applications, as outlined recently by Boldyreva, see Fig. 34 [11]. Two of them, concretely in materials engineering and in synthesis of materials for medicine, are described within this work. The aim is to illustrate that the mechanochemical route applied in materials science can encompass very different fields of human activity.

Materials engineering

One of the frequently used procedures for preparation of advanced materials is mechanical alloying (MA). One of the greatest advances of MA is the synthesis of novel alloys, e.g. alloying of normally immiscible elements, which is not possible by any other technique [4]. As an example, Al–Ni system can be described. The ultimate solubility of Al in Ni is 13.5 at.% at 1000 °C. The solubility decreases by a factor of 3.5 at 500 °C and becomes fractions of a per cent at room temperature. Nevertheless, the MA method enabled the preparation of solid solution of Al in Ni with aluminium content as high as 28 at.% [177]. The MA products find applications in preparation of various materials, as illustrated in Fig. 35.

Besides synthesis of new materials, also their reprocessing is attractive at the end of the day. It has

Table 4 Surface properties of the As_4S_4/ZnS nanocomposite. Reprinted with permission from Ref. [175]. Copyright 2017, Elsevier

As_4S_4/ZnS	S_A ($m^2.g^{-1}$)	Total pore volume ($cm^3.g^{-1}$)	Average pore diameter (nm)
5:0	0.3	0.0034	52.78
4:1	11	0.0837	29.74
1:1	11	0.0417	14.93
1:4	68	0.1039	6.09
0:5	126	0.1544	4.90

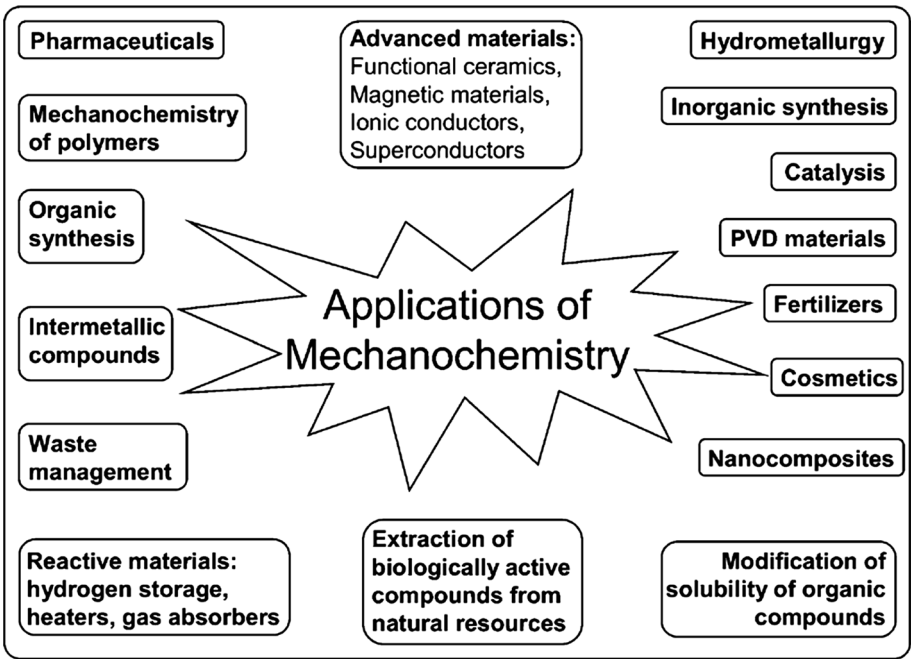

Figure 34 Applications of mechanochemistry. Reprinted with permission from Ref. [11]. Copyright 2013, Royal Society of Chemistry.

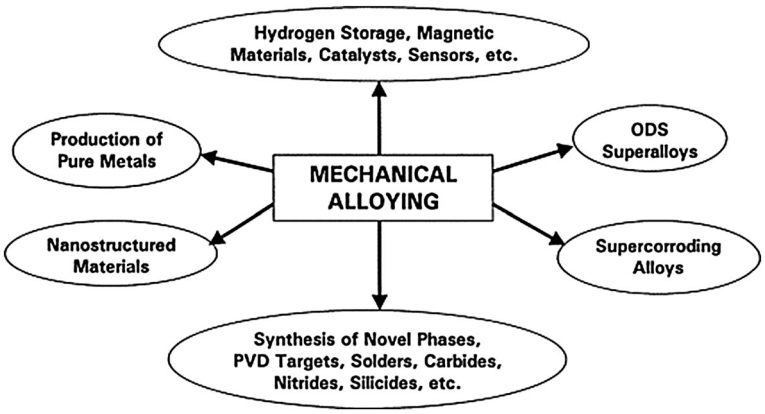

Figure 35 Typical current and potential future applications of materials synthesized by mechanical alloying. Reprinted with permission from Ref. [178]. Copyright 2001, Elsevier.

been shown that mechanochemical methods can also be applied for obtaining rare metals from waste, such as used television and computer monitors, displays, light bulbs. Compounds of europium, lanthanum, cerium and terbium play an active role in the luminescence-using equipment. Even short-term mechanochemical intervention facilitated the further processing steps [5, 179].

Materials for medicine

New trends in medicine can be traced in recent years. Nanotechnology with its broad spectrum of application penetrates into medicine more and more intensively. Among many nanotechnological products, chalcogenide quantum dots are gaining attention, mainly in connection with cancer management. Nanoparticles can be generated also by mechanochemical synthesis, which is the main topic of this review. In this part, few examples of application in medicine connected with bioimaging and cancer treatment are mentioned.

Bioimaging

Bioimaging is one of the pre-surgery steps in medicine, which searches for early symptoms of disease. This procedure is based on optical properties of applied materials. The high surface-to-volume ratio in nanocrystalline chalcogenides suggests the surface properties may play a significant role in optical properties of these materials [180]. These superior

optical properties and non-toxicity of chalcogenide nanocrystals give these materials a chance to be applied in bioimaging agenda and a significant advantage over conventional small-molecule dyes. As an example, broadly studied CdSe/ZnS system can be mentioned. Capping of bioimaging adept CdSe with a wider band gap semiconductor ZnS increases its quantum efficiency by removing the surface non-saturated trapping states of CdSe. For CdSe/ZnS, the reported room-temperature yield of fluorescence was 50% [181]. Moreover, this synthesis strategy can improve the stability of CdSe against the photo-oxidation and hinder the formation of toxic soluble cadmium species.

In recent years, several excellent reviews, in which a rich plethora of further inorganic nanoparticles and their combinations for the application in cell imaging and other bioapplications, like bio-tracking of drug molecules, biosensing and molecular biology, have been published [182–185]. However, the application of mechanochemical synthesis for their preparation is scarce.

InAs/ZnS The bioimaging properties of mechanochemically prepared InAs/ZnS nanocrystals were tested. For the determination of the properties in a biological system, it was necessary to prepare the samples in a form of nanosuspension [173]. The wet milling has been applied for this purpose. As a surfactant, the chitosan-based solution was applied. During the milling process, the average particle size was gradually decreased (from 630 to 310 nm). The largest particles in microrange disappeared, and only those in nanorange remained. The successful preparation of nanosuspension was confirmed by the measurement of zeta potential (ZP) and FTIR spectra. According to ZP results, the values were shifted to stable area (to high positive values, up to +61 mV) after the milling procedure, which is a proof of the improved stability of the nanoparticles in a suspension. The shifts in amine, amide and hydroxyl groups in FTIR spectra suggested the possible interaction between chitosan and InAs/ZnS particles.

The fluorescent and subsequent possible bioimaging properties were studied using PL spectroscopy. The PL spectrum with the emission peak of ZnS located at 360 nm was recorded. This peak was attributed to the band edge. In the measured spectrum, also two weaker peaks were registered, concretely at 425 nm and 470 nm. These small peaks indicated point defects, such as vacancies, interstitial ions or surface defects [186, 187]. In vitro studies for the confirmation of bioimaging properties of the prepared nanosuspension were realized on four cancer cell lines, HCT116 (human colorectal carcinoma), HeLa (human cervical adenocarcinoma), Caco-2 (human colorectal adenocarcinoma) and MCF7 (human breast adenocarcinoma). The results from the fluorescence microscopy showed that the prepared nanocrystals definitely have fluorescent properties and that they passed through the cell membrane and surrounded the nucleus. The bioimaging ability of chitosan-coated InAs/ZnS nanocrystals in a case of HeLa cells is depicted in Fig. 36. Using the flow cytometry analysis, it was determined that the cell granularity rapidly increased because of cellular uptake of the nanoparticles into the cytoplasm. Contrary to the excellent fluorescent properties of InAs/ZnS nanocrystals, the relative

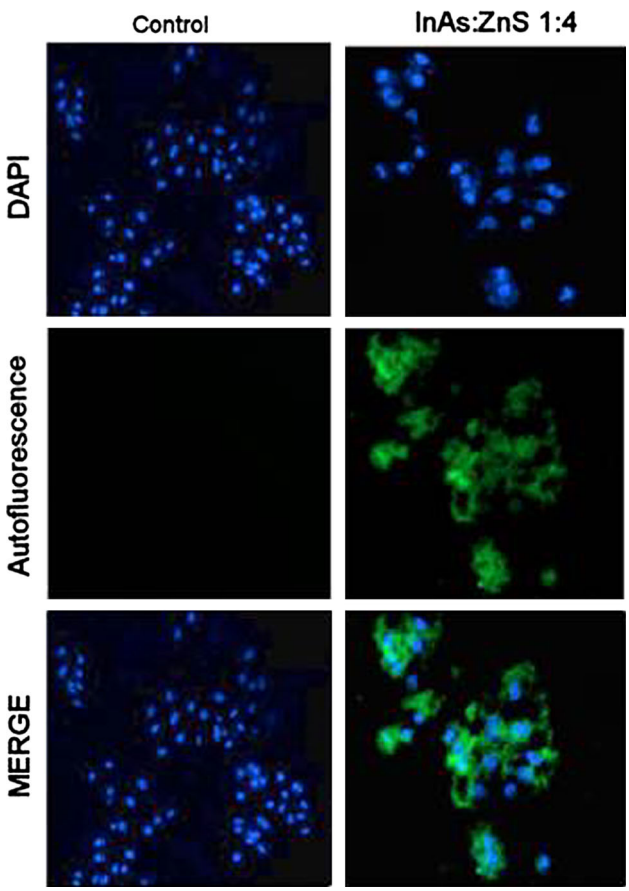

Figure 36 Fluorescence microscopy analysis of HeLa cancer cells after their treatment with chitosan-coated InAs/ZnS nanocrystals. Modified with permission from Ref. [173]. Copyright 2017, Springer.

viability of the cells was sharply decreasing with the increasing arsenic content (i.e. with the increasing amount of the applied nanocrystals). The cells were very sensitive to these nanocrystals, as even 1 $\mu g.mL^{-1}$ of arsenic concentration caused cell death. According to obtained results from in vitro studies, it was concluded that the nanosuspension had fluorescent properties. However, InAs/ZnS nanocrystals seemed to be highly toxic.

CdS/ZnS The nanosuspensions of CdS and CdS/ZnS nanocrystals were prepared by a mechanochemical route in a wet mode in cysteine- and polyvinylpyrrolidone (PVP)-based solutions [34]. Firstly, CdS and CdS/ZnS nanocrystals were prepared in a dry mechanochemical mode from the precursors, as was described in the paper [29]. After that, the wet milling process was applied, in order to obtain nanosuspensions suitable for in vitro testing of their biological properties and possible bioimaging applications. From the evolution of the particle size distribution, it was observed that upon milling in cysteine environment, particles became smaller. The distribution changed from polymodal to unimodal with the average size of 220 nm. The presence of the cysteine on the surface of these particles was sufficient to separate them and to avoid their aggregation. On the other hand, milling in PVP was not so effective, and the average particle size became larger and the obtained distribution was always polymodal. The zeta potential measurement was applied in order to observe the differences in a behaviour of the studied nanocrystals prepared using different capping agents. After the milling of CdS and CdS/ZnS nanocrystals in cysteine, the ZP was shifted to more negative values (up to −43 mV), which suggested good stability of the prepared nanosuspensions [188], provided through the electrostatic repulsion [189]. On the contrary, the ZP of the nanocrystals prepared in PVP was shifted to the less negative values (around 0 mV). In general, the stability is provided through steric stabilization when PVP is applied, and therefore, the decrease in ZP values does not mean the insufficient stability of nanosuspensions. However, in our case, this type of polymer was not appropriate to ensure the stability. The particle size was increased during the milling, and moreover, particles settled down few minutes after the milling process. The microenvironment and possible interactions between the particles and cysteine capping agent were studied using FTIR spectroscopy. The most important was to monitor the S–H bond vibration located at 2552 cm^{-1} in cysteine spectrum. In the case of CdS/ZnS system, this vibration has completely disappeared, as a consequence of utilization of this bond for the nanocrystals binding with cysteine. The optical properties of the prepared nanosuspensions were studied in order to determine their possible imaging abilities. In the case of CdS and CdS/ZnS nanosuspensions prepared in cysteine, the measured intensity of PL spectra of the nanosuspension containing mixed nanocrystals was higher in comparison with that with the pure CdS. This should come from the luminescence effect of the ZnS present in the CdS/ZnS nanocrystals. In the case of nanosuspensions prepared in PVP, the intensities were lower in comparison with that prepared in cysteine. The enhanced luminescence properties in the latter case were due to the surface modifications by cysteine molecules, with the effect of minimizing surface defects and enhancing the possibility of electron–hole recombination. The bioimaging properties and the metabolic activity were tested on four cancer cell lines (HeLa, Caco-2, HCT116 and MCF-7), similarly as in the case of InAs/ZnS–chitosan system. In comparison with InAs/ZnS nanosuspension, the metabolic activity of the cells was not significantly affected. However, it seemed that the slight differences between cysteine and PVP nanosuspensions exist. PVP nanosuspension was somewhat more toxic, but, on the other hand, the penetration of nanocrystals dispersed in this polymer through the cell membrane was more effective. In all cases, the nanocrystals showed autofluorescence, which opens the possibility to study their migration in cells. The nanocrystals entered the cell membrane, diffused through the cytoplasm and surrounded nucleus without further interfering with it. The changes in granularity were noticed as a consequence of the effective nanocrystals uptake. The example of bioimaging ability of CdS/ZnS nanosuspension is shown in Fig. 37. The small size and increased photostability of the nanocrystals support their use as nanoparticle-based cell imaging tool.

Cancer treatment

As_4S_4 Arsenic minerals have been used in traditional Chinese medicine for a very long time [190]. Among them, realgar As_4S_4 plays a special role

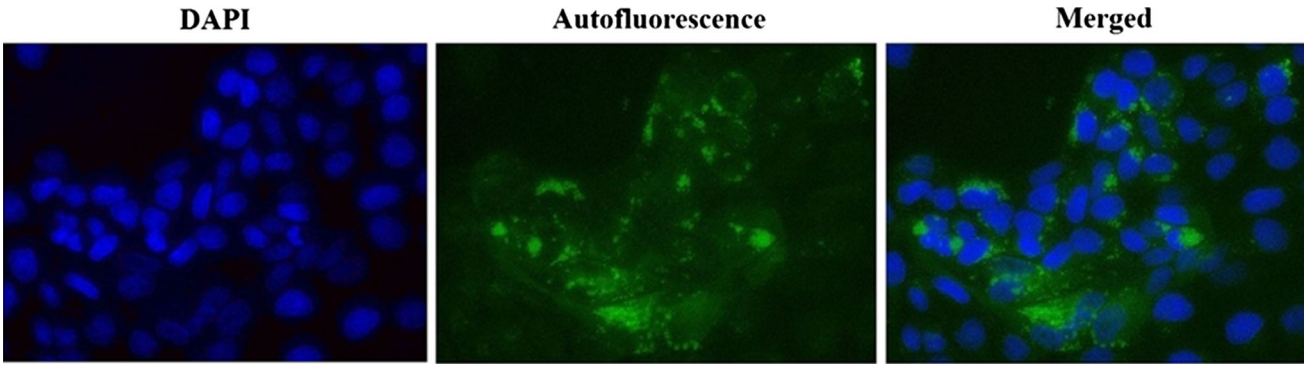

Figure 37 Fluorescent microscopy analysis of Caco-2 cancer cells after their treatment with CdS/ZnS nanocrystals dispersed in PVP. Modified with permission from Ref. [34]. Copyright 2017, Elsevier.

[191, 192]. Because of its low solubility, and in consequence bioavailability, the milling seemed to be an effective pre-treatment procedure to improve these properties. As_4S_4 particles were modified by milling, and the obtained nanoparticles were tested for the treatment of selected cancer cell lines.

In our early research regarding arsenic sulphides as curative agents, the samples were milled in a high-energy planetary ball mill. The milling was performed in a water solution of sodium dodecyl sulphate as a surfactant [193, 194]. The biological activity was tested on various cancer cell lines like U266, ARH77, K562, HL60, OPM1 and RPMI-LR5. The IC_{50} values (IC_{50} is the concentration that is required for 50% inhibition of cancer cells) were followed, with the result that they decreased in the case of multiple myeloma lines OPM1 and RPMI-LR5 with the increasing milling time (i.e. with the increasing specific surface area) of As_4S_4. In the case of OPM1 cells, the IC_{50} values were much lower in comparison with RPMI-LR5, meaning that this line was resistant to arsenic sulphides. The transmembrane mitochondrial potential (MTP) was also studied. For OPM1 cells, the decrease in this parameter was observed for the milled samples. For the RPMI-LR5 cell line, the MTP was more or less at the same level, regardless of milling.

In the paper [195], the arsenic sulphides were prepared in a form of nanosuspensions in the presence of 0.5% polyvinylpyrrolidone (PVP) as a non-ionic stabilizer. The determination of cytotoxicity was established on H460 human lung cancer cell line. The IC_{50} values were measured, and the low values were observed (see Table 5). As it can be seen, the values obtained for the non-milled samples were obviously higher (0.22 $\mu g.mL^{-1}$). The nanonization of the samples resulted in a higher toxicity to H460 cancer cells. The results were also compared with the *cis*-platin, which is used in medical practice as a standard anticancer drug. In this case, the obtained value was 0.01 $\mu g\ mL^{-1}$, which is very close to our results obtained for the milled samples. From the data in Table 5, it is clear that results obtained for milled realgar are comparable to those of standard anticancer drugs.

Table 5 IC_{50} values for various arsenic compounds to H460 cancer cells

Compound	IC_{50} ($\mu g\ mL^{-1}$)
As_4S_4 (realgar, non-milled)	0.22 ± 0.007
As_4S_4 (realgar, milled)	0.033 ± 0.007
As_4S_4 (pararealgar, milled)	0.031 ± 0.001
As_2O_3 (ATO)	0.050 ± 0.003
Cis-platin	0.010 ± 0.001

Reprinted with permission from Ref. [4]. Copyright 2014, Wiley–VCH

As_4S_4/ZnS The anticancer effect of binary As_4S_4/ZnS composites prepared in different As_4S_4:ZnS molar ratio was tested on two human melanoma cancer cell lines (A375 and Bowes). The composites were prepared as nanosuspensions in ultra-fine stirring mill in the presence of Poloxamer 407 (PX407) as a non-ionic surfactant [175]. All the samples exhibited concentration-dependent toxicity with increasing cytotoxic effect. According to IC_{50} results, the most toxic samples were As_4S_4/ZnS-PX407 1:1 and 1:4 for A375 cell line and As_4S_4/ZnS-PX407 1:1 for Bowes cell line. The cell cycle analysis for both cell lines revealed a concentration-dependent decrease in the proportion of G1 cells, which was accompanied by the accumulation of cells in G2/M phase of the cell

cycle. The detected anticancer effects on human melanoma cell lines A375 and Bowes confirmed high toxicity of the studied arsenic sulphides with the improved biological activity in the case of samples which contained admixture of zinc sulphide. Cell cycle in Bowes cells was more readily modulated than in A375 cells. In general, the cell cycle as a whole was a very sensitive parameter.

Scaling

Mechanochemical synthesis offers innovative approaches, in which the improvement in technological processes can be attained via contribution of several effects. The key aspect is the proper selection of a high-energy industrial mill, which serves as a mechanochemical reactor [3]. Scaling of the milling process requires activities in optimizing the design of the mill and its operation parameters. This process is very well elaborated in minerals engineering and hydrometallurgy, where traditional ball mills are increasingly being replaced by more energy-efficient mills [1, 196]. Various vertical and horizontal stirred ball mills were developed, which can be also perspectively applied in materials industry. Horizontal stirred ball mills (IsaMill^{TM}) have gone the successful way of scaling from laboratory to full-scale production. Up to today, 85% of all IsaMill^{TM} applications are processing of Pt group metals (40%), Cu/Au ores and Pb/Zn ores (22% each) [196, 197]. The largest machine size executed so far is M10000 IsaMill^{TM} (Fig. 38) with internal volume of 10 m^3 [196]. The mill is in plant operations in Australia and Kazakhstan. The mill with internal volume of 50 m^3 is under development.

In materials engineering, the eccentric vibratory mills are operating for mechanochemical synthesis of chalcogenides. This is particularly appealing, since it can substitute the pyrometallurgical production of these materials. The mills available from Siebtechnik GmbH are in modular design, which enables the adaptation of the mill capacity for the corresponding processes. Figure 39 shows an eccentric vibration mill (ESM) with a milling chamber with volume 150 L. The possible amount of milled material in this mill is up to 50 kg in a batch trial.

Computer simulation of a plant for mechanical synthesis of chalcogenides is provided in Fig. 40. The system has been designed for batch operation.

The mill has been tested for mechanochemical synthesis of several chalcogenide materials, which will be illustrated below. The satellite chamber with internal volume 5 litres attached to the mill has been applied in this case.

PbS While mechanochemical synthesis from elements (Pb, Zn, Se) has been applied in the previous examples, for the synthesis of PbS, the acetate route (see also part 2, Fig. 1b) was used [115]. The corresponding XRD patterns are given in Fig. 41. The resulting phase is lead sulphide PbS (JCPDS 5-592) with calculated crystallite size 13.4 nm. The size of PbS nanocrystals synthesized in an industrial mill is comparable with values obtained in laboratory mill, as reported in [38].

The importance of milling regime is illustrated in Fig. 42. In the batch experiment, 50 kg of input material (Cd and S), zirconia and steel balls and

Figure 38 M10000 IsaMill^{TM} [198].

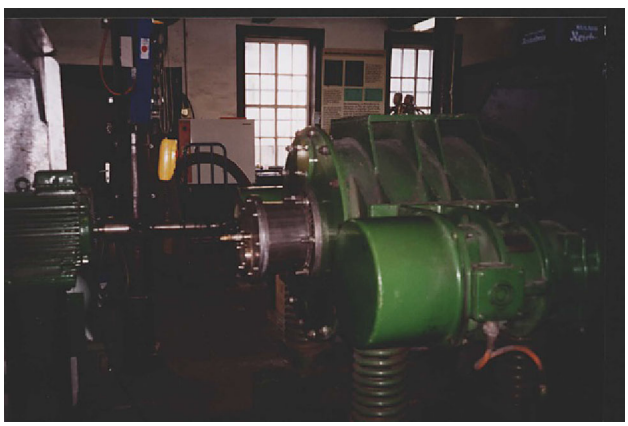

Figure 39 Eccentric pilot scale vibratory mill ESM 656–0.5 ks [199].

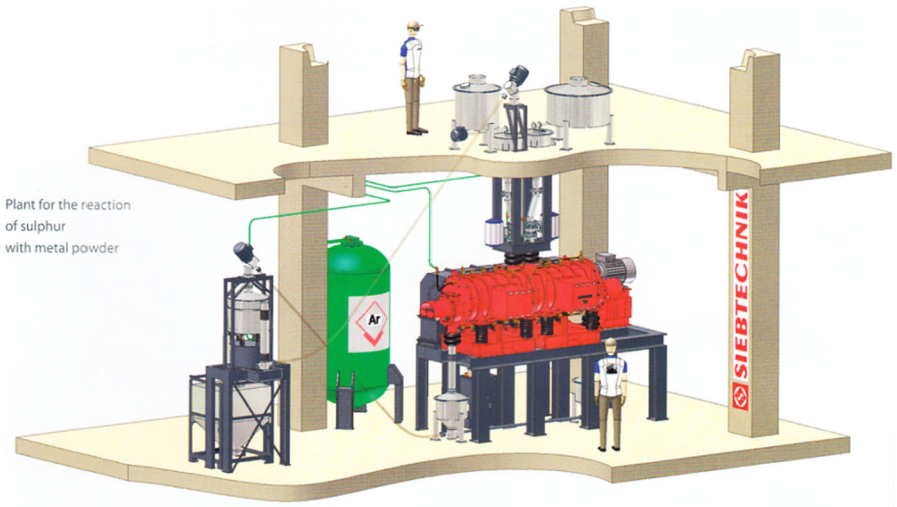

Figure 40 Plant for mechanochemical synthesis in a water-cooled ESM mill under inert atmosphere (computer simulation) [199].

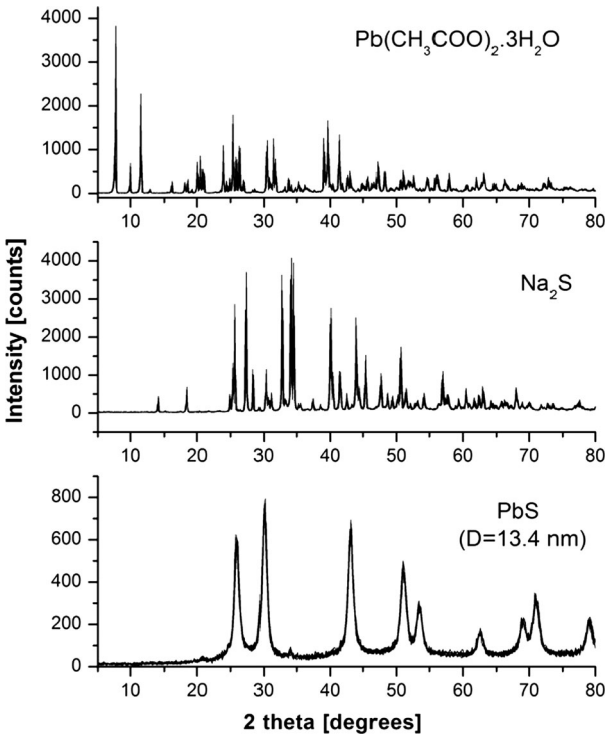

Figure 41 XRD patterns of mechanochemically synthesized lead sulphide PbS and precursors of the synthesis. Reprinted with permission from Ref. [115]. Copyright 2006, Elsevier.

milling time 20 and 120 min, respectively, have been evaluated as milling parameters. With the higher reaction time, amorphization of particles appears due to the disordering of the formed CdS phase. However, the utilization of Fe balls at lower times did not produce clean CdS products, as non-reacted Cd and S (not marked) are still present.

The applied eccentric vibratory mill is suitable for the mechanochemical synthesis of nanocrystalline semiconductors. Its theoretical evaluation and practical applications have been evaluated in works of late Professor Gock from Technical University of Clausthal, Germany, for the first time. Practically no wear during milling was detected. These results are important from the viewpoint of further compaction of the product and demands on semiconductor purity. It has been shown previously that the substantial reduction of specific power consumption, in comparison with other types of industrial mills, was obtained [200].

ZnSe The reaction between elemental zinc and selenium was performed within the work [201]. The XRD analysis of reaction products after 60 min of milling in the industrial mill has identified cubic ZnSe phase (stilleite, 37-1463) with the weak diffractions corresponding to the unreacted Zn phase (Fig. 43a). The calculated crystallite size using a reflection of ZnSe (111) plane was 10 nm, i.e. smaller in comparison with a crystallite size 21 nm for ZnSe produced in the laboratory mill [83, 201]. TEM study showed large agglomerates (clusters) of ZnSe nanoparticles having a size from about 100 to 500 nm (Fig. 43b). Such firmly bonded clusters of ZnSe nanoparticles showed no absorption edge in the UV–Vis optical absorption spectrum.

PbSe The XRD pattern of PbSe (clausthalite, JCPDS 6-354), mechanochemically synthesized for 12 min from elements, is shown in Fig. 44a. The process was also fast and effective in the industrial mill, as the degree of conversion to PbSe was 97% already after

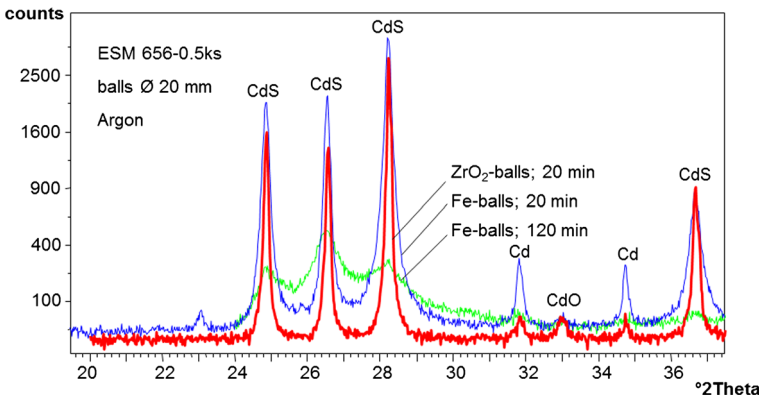

Figure 42 XRD pattern of CdS, mechanochemically synthesized in an industrial mill [199].

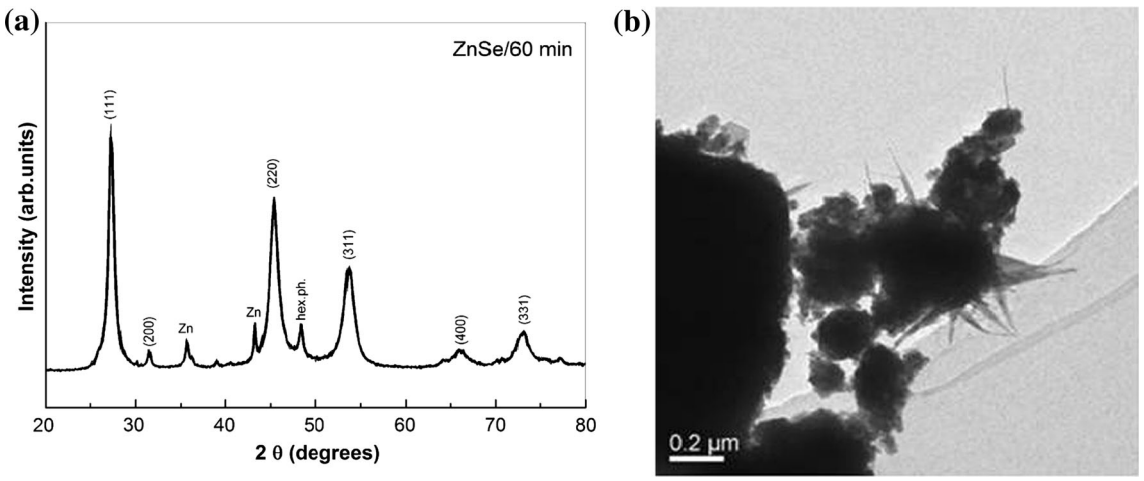

Figure 43 XRD pattern (**a**) and TEM image (**b**) of mechanochemically synthesized ZnSe.

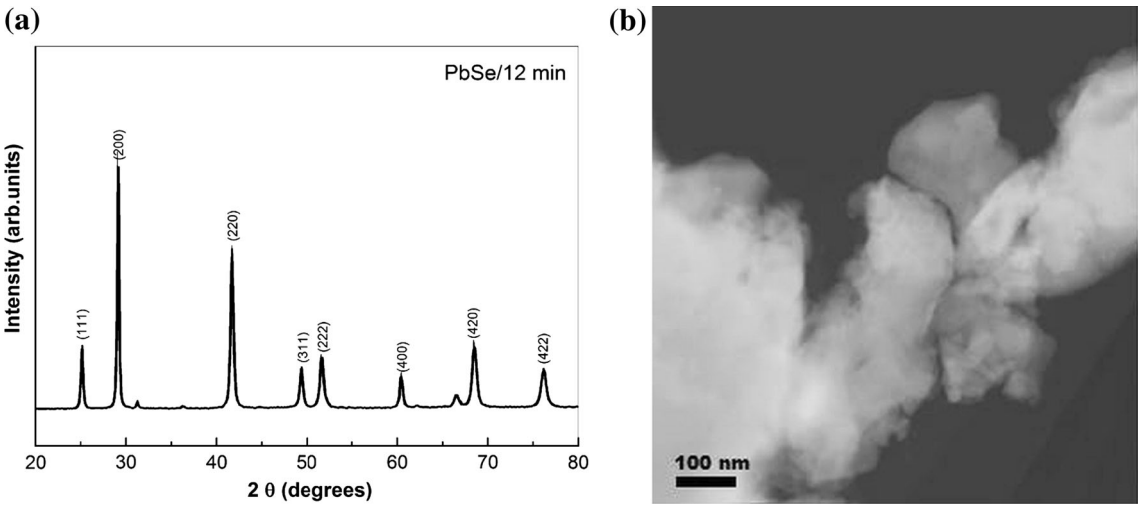

Figure 44 XRD pattern (**a**) and STEM image (**b**) of mechanochemically synthesized PbSe.

6 min of milling [83, 202]. The STEM image in Fig. 44b illustrates the smaller and bigger irregularly shaped PbSe nanoparticles situated in the clusters ranging in size from 0.2 to 1.0 μm, which could not be broken ultrasonically into single nanoparticles.

Conclusions

This paper attempted to provide an overview of the mechanochemical syntheses of chalcogenides in the last decade. Mechanochemical approach represents the top-down technique for preparation of substances in nanoscale. Chalcogenides exhibit variety of physical and chemical properties. For energy materials like chalcogenides, their high carrier mobility, large band gap and good photovoltaic properties represent a promising challenge. The preparation of chalcogenides in nanoscale as quantum dots broadens their application also for medicinal applications, concretely for imaging and cancer treatment.

All the above-mentioned aspects have been described in this paper on examples of binary, ternary and quaternary chalcogenide nanocrystals synthesized mechanochemically. The synthesis from elements, as well as from compounds was reviewed. The bio-inspired synthesis of nanocrystals and chalcogenide nanocomposites represents a challenge, as the materials applicable into living organisms are synthesized, where toxicity and hydrophobicity still represent a serious problem. Therefore, binary composites with non-toxic ZnS as a second component are being synthesized, which brings an improvement into this topic.

The paper describes the applications in materials engineering, bioimaging and cancer treatment. The possibility of scaling of mechanochemical synthesis is also illustrated. The main advantages of this approach are the decrease in the number of technological stages, the exclusion of operations that involve the use of solvents and gases and the possibility of obtaining products in the metastable state, which are difficult to obtain using traditional technological procedures. The environmental aspects of these processes are particularly attractive.

Acknowledgements

The present paper would not exist without the financial support of the Slovak Research and Development Agency under the Contract No. APVV-14-0103. The support of Slovak Grant Agency VEGA (Project 2/0027/14) and of German Federal Ministry of Education and Research (Project IB-COMSTRUC-010) is also gratefully acknowledged. The authors would like to thank Dr. N. Daneu and Dr. A. Feldhoff for the unpublished TEM images of presented metal selenides.

Compliance with ethical standards

Conflict of interest The authors declare that they have no conflict of interest.

References

[1] Baláž P (2008) Mechanochemistry in nanoscience and minerals engineering. Springer, Berlin Heidelberg

[2] Baláž P, Achimovičová M, Baláž M et al (2013) Hallmarks of mechanochemistry: from nanoparticles to technology. Chem Soc Rev 42:7571–7637

[3] Baláž P, Baláž M, Achimovičová M, Bujňáková Z, Dutková E (2014) Mechanochemistry of solids: new prospects for extractive metallurgy, materials science and medicine. Acta Phys Pol A 126:879–883

[4] Baláž P, Baláž M, Bujňáková Z (2014) Mechanochemistry in technology: from minerals to nanomaterials and drugs. Chem Eng Technol 37:747–756

[5] Baláž P, Dutková E (2009) Fine milling in applied mechanochemistry. Miner Eng 22:681–694

[6] Urakaev FK (2013) Phenomenology, mechanism and kinetics of the combustion reactions in mechanochemical reactors for the example of Zn–S–Sn system processing in a ball mill (overview). Int J Comput Mater Sci Surf Eng 5:224–261

[7] Šepelák V, Düvel A, Wilkening M, Becker KD, Heitjans P (2013) Mechanochemical reactions and syntheses of oxides. Chem Soc Rev 42:7507–7520

[8] Takacs L (2013) The historical development of mechanochemistry. Chem Soc Rev 42:7649–7659

[9] Burmeister CF, Kwade A (2013) Process engineering with planetary ball mills. Chem Soc Rev 42:7660–7667

[10] Ralphs K, Hardacre C, James SL (2013) Application of heterogeneous catalysts prepared by mechanochemical synthesis. Chem Soc Rev 42:7701–7718

[11] Boldyreva E (2013) Mechanochemistry of inorganic and organic systems: What is similar, what is different? Chem Soc Rev 42:7719–7738

[12] Friščić T (2010) New opportunities for materials synthesis using mechanochemistry. J Mater Chem 20:7599–7605

[13] Zhu SE, Li F, Wang GW (2013) Mechanochemistry of fullerenes and related materials. Chem Soc Rev 42:7535–7570

[14] Wang GW (2013) Mechanochemical organic synthesis. Chem Soc Rev 42:7668–7700

[15] James SL, Adams CJ, Bolm C et al (2012) Mechanochemistry: opportunities for new and cleaner synthesis. Chem Soc Rev 41:413–447

[16] Stolle A, Szuppa T, Leonhardt SES, Ondruschka B (2011) Ball milling in organic synthesis: solutions and challenges. Chem Soc Rev 40:2317–2329

[17] Baláž P, Dutková E (2007) Mechanochemistry of sulphides: from minerals to advanced nanocrystalline materials. J Therm Anal Calorim 90:85–92

[18] Urakaev FK (2011) Scientific principles for preparation nanoscale particles by the exchange mechanochemical reactions (overview). Int J Comput Mater Sci Surf Eng 4:347–373

[19] Braga D, Maini L, Grepioni F (2013) Mechanochemical preparation of co-crystals. Chem Soc Rev 42:7638–7648

[20] Šepelák V, Becker KD (2012) Mechanochemistry: from mechanical degradation to novel materials properties. J Korean Ceram Soc 42:19–28

[21] James SL, Friscic T (2013) Mechanochemistry. Chem Soc Rev 42:7494–7496

[22] May PA, Moore JS (2013) Polymer mechanochemistry: techniques to generate molecular force via elongational flows. Chem Soc Rev 42:7497–7506

[23] Cravotto G, Gaudino EC, Cintas P (2013) On the mechanochemical activation by ultrasound. Chem Soc Rev 42:7521–7534

[24] Friscic T (2012) Supramolecular concepts and new techniques in mechanochemistry: cocrystals, cages, rotaxanes, open metal-organic frameworks. Chem Soc Rev 41:3493–3510

[25] Šepelák V, Begin-Colin S, Le Caer G (2012) Transformations in oxides induced by high-energy ball-milling. Dalton Trans 41:11927–11948

[26] Brion D (1980) Etude par spectroscopie de photoelectrons de la degradation superficielle de FeS_2, $CuFeS_2$, ZnS et PbS a Íair et dans Íeau. Appl Surf Sci 5:132–152

[27] Baláž P (2000) Extractive metallurgy of activated minerals. Elsevier, Amsterdam

[28] Baláž P, Boldižárová E, Godočíková E, Briančin J (2003) Mechanochemical route for sulphide nanoparticles preparation. Mater Lett 57:1585–1589

[29] Baláž P, Baláž M, Dutková E et al (2016) CdS/ZnS nanocomposites: from mechanochemical synthesis to cytotoxicity issues. Mater Sci Eng C 58:1016–1023

[30] Baláž P, Sayagués MJ, Baláž M et al (2014) CdSe@ZnS nanocomposites prepared by a mechanochemical route: no release of Cd^{2+} ions and negligible in vitro cytotoxicity. Mater Res Bull 49:302–309

[31] Baláž P, Jardin R, Dutková E et al (2012) Mechanochemical synthesis and characterization of II–VI nanocrystals: challenge for cytotoxicity issues. Acta Phys Pol A 122:224–229

[32] Baláž P, Pourghahramani P, Dutková E, Fabián M, Kováč J, Šatka A (2009) PbS nanostructures synthesized via surfactant assisted mechanochemical route. Cent Eur J Chem 7:215–221

[33] Dutková E, Baláž P, Pourghahramani P, Velumani S, Ascencio JA, Kostova NG (2009) Properties of mechanochemically synthesized ZnS nanoparticles. J Nanosci Nanotechnol 9:6600–6605

[34] Bujňáková Z, Baláž M, Dutková E et al (2017) Mechanochemical approach for the capping of mixed core CdS/ZnS nanocrystals: elimination of cadmium toxicity. J Colloid Interface Sci 486:97–111

[35] Baláž P, Baláž M, Čaplovičová M, Zorkovská A, Čaplovič Ľ, Psotka M (2014) The dual role of sulfur-containing amino acids in the synthesis of IV–VI semiconductor nanocrystals: a mechanochemical approach. Faraday Discuss 170:169–179

[36] Baláž M, Baláž P, Tjuliev G et al (2013) Cystine-capped CdSe@ZnS nanocomposites: mechanochemical synthesis, properties, and the role of capping agent. J Mater Sci 48:2424–2432. doi:10.1007/s10853-012-7029-3

[37] Dutková E, Baláž P, Pourghahramani P et al (2012) Mechanochemically synthesised $Zn_xCd_{1-x}S$ nanoparticles for solar energy applications. J Nano Res 18–19:247–256

[38] Baláž P, Pourghahramani P, Achimovičová M et al (2011) Mechanochemical synthesis and reactivity of PbS nanocrystals. J Cryst Growth 332:1–6

[39] Baláž P, Škorvánek I, Fabián M et al (2010) Properties of magnetically diluted nanocrystals prepared by mechanochemical route. J Alloys Compd 504:S340–S344

[40] Dutková E, Baláž P, Pourghahramani P (2009) CdS nanoparticles mechanochemically synthesized in a high-energy mill. J Optoelectron Adv Mater 11:2102–2107

[41] Dutková E, Baláž P, Pourghahramani P et al (2008) Mechanochemical solid state synthesis and characterization of $Cd_xZn_{1-x}S$ nanocrystals. Solid State Ion 179:1242–1245

[42] Dutková E, Takacs L, Sayagués MJ, Baláž P, Kováč J, Šatka A (2013) Mechanochemical synthesis of Sb_2S_3 and Bi_2S_3 nanoparticles. Chem Eng Sci 85:25–29

[43] Dutková E, Sayagues MJ, Zorkovská A et al (2014) Properties of mechanochemically synthesized

nanocrystalline Bi_2S_3 particles. Mater Sci Semicond Process 27:267–272

[44] Zhao WB, Zhu JH, Zhao Y, Chen HY (2004) Photochemical synthesis and characterization of Bi_2S_3 nanofibers. Mater Sci Eng B 110:307–313

[45] Nayak BB, Acharya HN, Mitra GB, Mathur BK (1983) Structural characterization of $Bi_{2-x}Sb_xS_3$ films prepared by the dip-dry method. Thin Solid Films 105:17–24

[46] Spanhel L, Anderson MA (1990) Synthesis of porous quantum-size CdS membranes—photoluminescence phase-shift and demodulation measurements. JACS 112:2278–2284

[47] Zhao LD, Zhang BP, Liu WS, Zhang HL, Li JF (2008) Enhanced thermoelectric properties of bismuth sulfide polycrystals prepared by mechanical alloying and spark plasma sintering. J Solid State Chem 181:3278–3282

[48] Dutková E, Sayagués MJ, Real C et al (2014) Mechanochemically synthesized nanocrystalline Sb_2S_3 particles. Acta Phys Pol A 126:943–946

[49] Calka A, Mosbah A, Stanford N, Baláž P (2008) Rapid synthesis of Bi and Sb sulfides using electric discharge assisted mechanical milling. J Alloys Compd 455:285–288

[50] Vaughan DJ, Craig JR (1978) Mineral chemistry of metal sulfides. Cambridge University Press, Cambridge

[51] Roy P, Srivastava SK (2015) Nanostructured copper sulfides: synthesis, properties and applications. CrystEngComm 17:7801–7815

[52] Shamraiz U, Hussain RA, Badshah A (2016) Fabrication and applications of copper sulfide (CuS) nanostructures. J Solid State Chem 238:25–40

[53] Goel S, Chen F, Cai WB (2014) Synthesis and biomedical applications of copper sulfide nanoparticles: from sensors to theranostics. Small 10:631–645

[54] Xiao ZY (2014) CuS nanoparticles: clinically favorable materials for photothermal applications? Nanomedicine 9:373–375

[55] Tschakarov CG, Gospodinov GG, Bontschev Z (1982) Über den Mechanismus der mechanochemischen Synthese anorganischer Verbindungen. J Solid State Chem 41:244–252

[56] Ohtani T, Motoki M, Koh K, Ohshima K (1995) Synthesis of binary copper chalcogenides by mechanical alloying. Mater Res Bull 30:1495–1504

[57] Blachnik R, Muller A (2000) The formation of Cu_2S from the elements I. Copper used in form of powders. Thermochim Acta 361:31–52

[58] Wang K, Tan GL (2010) Synthesis and optical properties of CuS nanocrystals by mechanical alloying process. Curr Nanosci 6:163–168

[59] Kristl M, Ban I, Gyergyek S (2013) Preparation of nano-sized copper and cadmium chalcogenides by mechanochemical synthesis. Mater Manuf Processes 28:1009–1013

[60] Ou Z, Li J (2014) Synergism of mechanical activation and sulfurization to recover copper from waste printed circuit boards. RSC Adv 4:51970–51976

[61] Li S, Ge ZH, Zhang BP et al (2016) Mechanochemically synthesized sub-5 nm sized CuS quantum dots with high visible-light-driven photocatalytic activity. Appl Surf Sci 384:272–278

[62] Baláž M, Zorkovská A, Urakaev F et al (2016) Ultrafast mechanochemical synthesis of copper sulfides. RSC Adv 6:87836–87842

[63] Liu XJ, Li B, Fu FF et al (2014) Facile synthesis of biocompatible cysteine-coated CuS nanoparticles with high photothermal conversion efficiency for cancer therapy. Dalton Trans 43:11709–11715

[64] Zhou M, Song SL, Zhao J, Tian M, Li C (2015) Theranostic CuS nanoparticles targeting folate receptors for PET image-guided photothermal therapy. J Mater Chem B 3:8939–8948

[65] Rusanov V, Chakurov C (1990) Percolation phenomena in explosive mechanochemical synthesis of some metal chalcogenides. J Solid State Chem 89:1–9

[66] Chakurov C, Rusanov V, Koichev J (1987) The effect of inert additives on the explosive mechanochemical synthesis of some metal chalcogenides. J Solid State Chem 71:522–529

[67] Takacs L (2002) Self-sustaining reactions induced by ball milling. Prog Mater Sci 47:355–414

[68] Takacs L (2010) In: Sopicka-Lizer M (ed) High-energy ball milling: mechanohemical processing of nanopowders. Woodhead Publishing Limited, Oxford

[69] Takacs L (2014) Gradual and self-sustaining processes in the Sn–Zn–Se system. Acta Phys Pol A 126:1032–1039

[70] Takacs L (2014) Self-sustaining reactions as a tool to study mechanochemical activation. Faraday Discuss 170:251–265

[71] Avvakumov EG (1979) Methods in chemical processes activation. Nauka, Novosibirsk

[72] Faita FL, Ersching K, Poffo CM et al (2014) Structural, thermal, magnetic and optical characterization of undoped nanocrystalline ZnS prepared by solid state reaction. J Alloys Compd 590:176–183

[73] Farooqi MMH, Srivastava RK (2014) Structural, optical and photoconductivity study of ZnS nanoparticles synthesized by a low temperature solid state reaction method. Mater Sci Semicond Process 20:61–67

[74] Trajić J, Kostić R, Romčević N et al (2015) Raman spectroscopy of ZnS quantum dots. J Alloys Compd 637:401–406

[75] Trajić J, Romčević M, Romčević N, Babić B, Matović B, Baláž P (2016) Far-infrared spectra of mesoporous ZnS nanoparticles. Opt Mater 57:225–230

[76] Ohtani T, Ikeda K, Hayashi Y, Fukui Y (2007) Mechanochemical preparation of palladium chalcogenides. Mater Res Bull 42:1930–1934

[77] Urakaev FK (2013) Simulation of the mechanically induced self-propagating reactions: heat source of "viscous flow" and mechanism of MSR in Zn–S system. Combust Sci Technol 185:1281–1294

[78] Liu XJ, Xu ZZ, Xiao H et al (2014) The effect of process control agents and ball to powder rations on the electrochemical characteristics of mechanically alloyed SnS_2 anode materials. Powder Technol 259:117–124

[79] Tan Q, Li JF (2014) Thermoelectric properties of Sn–S bulk materials prepared by mechanical alloying and spark plasma sintering. J Electron Mater 43:2435–2439

[80] Wu ZZ, Wang DZ, Sun AK (2010) Preparation of MoS_2 by a novel mechanochemical method. J Alloys Compd 492:L5–L7

[81] Wu ZZ, Wang DZ, Zan XQ, Sun AK (2010) Synthesis of WS_2 nanosheets by a novel mechanical activation method. Mater Lett 64:856–858

[82] Abraham A, Zhong ZY, Liu RD et al (2016) Preparation, ignition, and combustion of Mg center dot S reactive nanocomposites. Combust Sci Technol 188:1345–1364

[83] Achimovičová M, Baláž P (2015) In: Ramirez M (ed) Milling fundamentals, processes and technologies. NOVA Science Publishers Inc., New York

[84] Wang H, Du F (2006) Hydrothermal synthesis of ZnSe hollow microspheres. Cryst Res Technol 41:323–327

[85] Eliyas A, Achimovičová M, Kostova N, Zorkovská A, Baláž P (2012) Photocataytic activity of thin film of cadmium selenide for air decontamination by complete oxidation of ethylene. Nanosci Nanotechnol 12:28–32

[86] Tan GL, Du JH, Zhang QJ (2009) Structural evolution and optical properties of CdSe nanocrystals prepared by mechanical alloying. J Alloys Compd 468:421–431

[87] Tan GL, Liu RH (2010) Preparation of pure CdSe nanocrystals through mechanical alloying. J Nanopart Res 12:605–614

[88] Ohtani T, Kusano Y, Ishimaru K, Morimoto T, Togano A, Yoshioka T (2015) Pre-milling effects on self-propagating reactions in mechanochemical synthesis of CdSe and ZnSe. Chem Lett 44:1234–1236

[89] Baltazar-Rodrigues J, de Lima JC, Campos CEM, Grandi TA (2009) Temperature effects on mechanically alloyed nanometric ZnSe powder. Powder Technol 189:70–73

[90] Gotor FJ, Achimovičová M, Real C, Baláž P (2013) Influence of the milling parameters on the mechanical work intensity in planetary mills. Powder Technol 233:1–7

[91] Sashchiuk A, Amirav L, Bashouti M, Krueger M, Sivan U, Lifshitz E (2004) PbSe nanocrystal assemblies: synthesis and structural, optical, and electrical characterization. Nano Lett 4:159–165

[92] Pejova B, Grozdanov I (2007) Chemical synthesis, structural and optical properties of quantum sized semiconducting tin(II) selenide in thin film form. Thin Solid Films 515:5203–5211

[93] Achimovičová M, Rečnik A, Daneu N, da Silva KL, Harvanová J (2011) Study of tin selenide mechanochemical synthesis. In: 11th international multidisciplinary scientific geoconference (SGEM 2011), vol II, p 745

[94] Achimovičová M, da Silva KL, Daneu N et al (2011) Structural and morphological study of mechanochemically synthesized tin diselenide. J Mater Chem 21:5873–5876

[95] Agarwal MK, Patel PD, Patel SS (1991) Growth of large size single-crystals of $SnSe_2$ using a direct transport method. J Cryst Growth 110:553–558

[96] George J, Kumari CKV (1986) Optical, electrical and morphological-studies of $SnSe_2$ crystals grown by physical vapor transport method. Cryst Res Technol 21:273–278

[97] Lee PA, Said G (1968) Optical properties of tin di-selenide single crystals. J Phys D Appl Phys 1:837–843

[98] El-Nahass MM (1992) Optical-properties of tin diselenide films. J Mater Sci 27:6597–6604.

[99] Achimovičová M, Gotor FJ, Real C, Daneu N (2012) Mechanochemical synthesis and characterization of nanocrystalline BiSe, Bi_2Se_3 semiconductors. J Mater Sci Mater Electron 23:1844–1850

[100] Liu FY, Wang B, Lai YQ, Li J, Zhang ZA, Liu YX (2010) Electrodeposition of cobalt selenide thin films. J Electrochem Soc 157:D523–D527

[101] Kristl M, Gyergyek S, Srt N, Ban I (2016) Mechanochemical route for the preparation of nanosized aluminium and gallium sulfide and selenide. Mater Manuf Processes 31:1608–1612

[102] Campos CEM, de Lima JC, Grandi TA, Souza SM, Pizani PS (2007) Age-induced phase transitions on mechanically alloyed amorphous GaSe. Solid State Commun 142:270–275

[103] de Souza SM, de Lima JC, Campos CEM, Grandi TA, Triches DM (2008) Ageing-induced structural evolution of mechanically alloyed $Ga_{40}Se_{60}$. J Phys Condens Matter 20

[104] Nunes RM, Campos CEM, Drago V, Grandi TA, de Lima JC (2010) Structural stability of mechanically alloyed TM25Se75 (TM = Fe, Co and Ni). J Non-Cryst Solids 356:1145–1148

[105] Zhang SN, Liu JX, Feng JQ et al (2015) Fabrication mechanism of FeSe superconductors milling aided sintering process with high-energy ball. Mater Chem Phys 163:587–593

[106] Zhang S, Liu J, Feng JX, Li C, Ma XX, Zhang P (2015) Optimization of FeSe superconductors with the high-energy ball milling aided sintering process. J Materiomics 1:118–123

[107] Hussain RA, Badshah A, Lal B (2016) Fabrication, characterization and applications of iron selenide. J Solid State Chem 243:179–189

[108] Achimovičová M, Daneu N, Dutková E, Zorkovská A (2017) Mechanochemically synthesized cobalt monoselenide: structural characterization and optical properties. Appl Phys A 123:154

[109] Tan GL, Hommerich U, Temple D, Wu NQ, Zheng JG, Loutts G (2003) Synthesis and optical characterization of CdTe nanocrystals prepared by ball milling process. Scr Mater 48:1469–1474

[110] Tan GL, Yang Q, Hommerich U, Seo JT, Temple D (2004) Linear and non-linear optical properties of capped CdTe nanocrystals prepared by mechanical alloying. Opt Mater 27:579–584

[111] Humphry-Baker SA, Garroni S, Delogu F, Schuh CA (2016) Melt-driven mechanochemical phase transformations in moderately exothermic powder mixtures. Nat Mater 15:1280–1286

[112] Campos CEM, Ersching K, de Lima JC, Grandi TA, Hohn H, Pizani PS (2008) Influence of minor oxidation of the precursor powders to form nanocrystalline CdTe by mechanical alloying. J Alloys Compd 466:80–86

[113] Campos CEM, de Lima JC, Grandi TA, Hohn H (2008) Synthesis of nanocrystalline zinc blende ZnTe by mechanical alloying. J Non-Cryst Solids 354:3503–3506

[114] Campos CEM (2014) Solid state synthesis and characterization of NiTe nanocrystals. J Nano Res 29:35–39

[115] Godočíková E, Baláž P, Gock E, Choi WS, Kim BS (2006) Mechanochemical synthesis of the nanocrystalline semiconductors in an industrial mill. Powder Technol 164:147–152

[116] Tolia JV, Chakraborty M, Murthy ZVP (2012) Mechanochemical synthesis and characterization of group II–VI semiconductor nanoparticles. Part Sci Technol 30:533–542

[117] Zan GT, Wu QS (2016) Biomimetic and bioinspired synthesis of nanomaterials/nanostructures. Adv Mater 28:2099–2147

[118] Huang JL, Lin LQ, Sun DH, Chen HM, Yang DP, Li QB (2015) Bio-inspired synthesis of metal nanomaterials and applications. Chem Soc Rev 44:6330–6374

[119] Zhou H, Fan TX, Li XF et al (2009) Bio-inspired bottom-up assembly of diatom-templated ordered porous metal chalcogenide meso/nanostructures. Eur J Inorg Chem 211–215

[120] Rao MD, Pennathur G (2016) Facile bio-inspired synthesis of zinc sulfide nanoparticles using *Chlamydomonas reinhardtii* cell free extract: optimization, characterization and optical properties. Green Process Synth 5:379–388

[121] Shen LM, Bao NZ, Prevelige PE, Gupta A (2010) Fabrication of ordered nanostructures of sulfide nanocrystal assemblies over self-assembled genetically engineered P22 coat protein. JACS 132:17354–17357

[122] Lu Y, Fong E (2016) Biomass-mediated synthesis of carbon-supported nanostructured metal sulfides for ultra-high performance lithium-ion batteries. J Mater Chem A 4:2738–2745

[123] Zhong RZ, Peng C, Chen L et al (2016) Egg white-mediated green synthesis of CuS quantum dots as a biocompatible and efficient 980 nm laser-driven photothermal agent. RSC Adv 6:40480–40488

[124] Su H, Han J, Wang N, Dong Q, Zhang D, Zhang C (2008) In situ synthesis of lead sulfide nanoclusters on eggshell membrane fibers by an ambient bio-inspired technique. Smart Mater Struct 17:art. no. 015045

[125] Pawar V, Kumar AR, Zinjarde S, Gosavi S (2013) Bioinspired inimitable cadmium telluride quantum dots for bioimaging purposes. J Nanosci Nanotechnol 13:3826–3831

[126] Baláž M, Baláž P, Sayagués MJ, Zorkovská A (2013) Bio-inspired mechanochemical synthesis of semiconductor nanomaterial using eggshell membrane. Mater Sci Semicond Process 16:1899–1903

[127] Baláž M (2014) Eggshell membrane biomaterial as a platform for the applications in materials science. Acta Biomater 10:3827–3843

[128] Su HL, Wang N, Dong Q, Zhang D (2006) Incubating lead selenide nanoclusters and nanocubes on the eggshell membrane at room temperature. J Membr Sci 283:7–12

[129] Kodali VK, Gannon SA, Paramasivam S, Raje S, Polenova T, Thorpe C (2011) A novel disulfide-rich protein motif from avian eggshell membranes. PLoS ONE 6:art. no. e18187

[130] Green MA, Emery K, King DL, Igari S, Warta W (2002) Solar cell efficiency tables (version 20). Prog Photovolt 10:355–360

[131] Djellal L, Bouguelia A, Trari M (2008) Physical and photoelectrochemical properties of p-$CuInSe_2$ bulk material. Mater Chem Phys 109:99–104

[132] Vanalakar SA, Agawane GL, Shin SW et al (2015) Non-vacuum mechanochemical route to the synthesis of

Cu_2SnS_3 nano-ink for solar cell applications. Acta Mater 85:314–321

[133] Dutková E, Sayagués MJ, Briančin J et al (2016) Synthesis and characterization of $CuInS_2$ nanocrystalline semiconductor prepared by high-energy milling. J Mater Sci 51:1978–1984. doi:10.1007/s10853-015-9507-x

[134] Li DS, Zou Y, Yang DR (2012) Controlled synthesis of luminescent $CuInS_2$ nanocrystals and their optical properties. J Lumin 132:313–317

[135] Wu SM, Xue YZ, Zhou LM, Liu X, Xu DY (2014) Structure and morphology evolution in mechanochemical processed $CuInS_2$ powder. J Alloys Compd 600:96–100

[136] Kim KH, Lee JK, Alphonse A et al (2013) Preparation of precursor particles by cryogenic mechanical milling for the deposition of $CuInS_2$ thin films. Mater Sci Semicond Process 16:226–230

[137] Li JH, Tan Q, Li JF (2013) Synthesis and property evaluation of $CuFeS_{2-x}$ as earth-abundant and environmentally-friendly thermoelectric materials. J Alloys Compd 551:143–149

[138] Shawky M, Shenouda A, El-sShreafy E, Ibrahim IA (2015) Synthesis, characterization and performance of Cu_2SnS_3 for solar cell application. Int J Sci Eng Res 6:1447–1453

[139] Dutková E, Sayagués MJ, Kováč J et al (2016) Mechanochemically synthesized nanocrystalline ternary $CuInSe_2$ chalcogenide semiconductor. Mater Lett 173:182–186

[140] Rincon C, Ramirez FJ (1992) Lattice-vibrations of $CuInSe_2$ and $CuGaSe_2$ by Raman microspectrometry. J Appl Phys 72:4321–4324

[141] Eisener B, Wagner M, Wolf D, Muller G (1999) Study of the intrinsic defects in solution grown $CuInSe_2$ crystals depending on the path of crystallization. J Cryst Growth 198:321–324

[142] Sabet M, Salavati-Niasari M, Ghanbari D, Amiri O, Mir N, Dadkhah M (2014) Synthesis and characterization of $CuInSe_2$ nanocrystals via facile microwave approach and study of their behavior in solar cell. Mater Sci Semicond Process 25:98–105

[143] Chen K, Du BL, Bonini N, Weber C, Yan HX, Reece MJ (2016) Theory-guided synthesis of an eco-friendly and low-cost copper based sulfide thermoelectric material. J Phys Chem C 120:27135–27140

[144] Zhang RZ, Chen K, Du B, Reece MJ (2017) Screening for Cu–S based thermoelectric materials using crystal structure features. J Mater Chem A 5:5013–5019

[145] Du BL, Zhang RZ, Chen K, Mahajan A, Reece MJ (2017) The impact of lone-pair electrons on the lattice thermal conductivity of the thermoelectric compound $CuSbS_2$. J Mater Chem A 5:3249–3259

[146] Hsu W, Sutter-Fella CM, Hettick M et al (2015) Electron-selective TiO_2 contact for Cu(In,Ga)Se-2 solar cells. Sci Rep 5

[147] Guo Q, Ford GM, Yang WC et al (2010) Fabrication of 7.2% efficient CZTSSe solar cells using CZTS nanocrystals. JACS 132:17384–17386

[148] Delbos S (2012) Kesterite thin films for photovoltaics: a review. EPJ Photovolt 3:art. no. 35004

[149] Song XB, Ji X, Li M, Lin WD, Luo X, Zhang H (2014) A review on development prospect of CZTS based thin film solar cells. Int J Photoenergy:art. no. 613173

[150] Scragg J (2011) Copper zinc tin sulfide thin films for photovoltaics. Springer, Berlin Heidelberg

[151] Siebentritt S, Schorr S (2012) Kesterites—a challenging material for solar cells. Prog Photovolt 20:512–519

[152] Ito K, Nakazawa T (1988) Electrical and optical-properties of stannite-type quaternary semiconductor thin-films. Jpn J Appl Phys Part 1 27:2094–2097

[153] Green MA, Emery K, Hishikawa Y, Warta W, Dunlop ED (2015) Solar cell efficiency tables (version 45). Prog Photovolt 23:1–9

[154] Pareek D, Balasubramaniam KR, Sharma P (2016) Reaction pathway for synthesis of $Cu_2ZnSn(S/Se)_4$ via mechano-chemical route and annealing studies. J Mater Sci Mater Electron 28:1199–1210

[155] Polman A, Knight M, Garnett EC, Ehrler B, Sinke WC (2016) Photovoltaic materials: present efficiencies and future challenges. Science 352:307

[156] Beecroft LL, Ober CK (1997) Nanocomposite materials for optical applications. Chem Mater 9:1302–1317

[157] Mokurala K, Bhargava P, Mallick S (2014) Single step synthesis of chalcogenide nanoparticles Cu_2ZnSnS_4, Cu_2FeSnS_4 by thermal decomposition of metal precursors. Mater Chem Phys 147:371–374

[158] Shyju TS, Anandhi S, Suriakarthick R, Gopalakrishnan R, Kuppusami P (2015) Mechanosynthesis, deposition and characterization of CZTS and CZTSe materials for solar cell applications. J Solid State Chem 227:165–177

[159] Park BI, Hwang Y, Lee SY et al (2014) Solvent-free synthesis of Cu_2ZnSnS_4 nanocrystals: a facile, green, up-scalable route for low cost photovoltaic cells. Nanoscale 6:11703–11711

[160] Wang Y, Gong H (2011) Cu_2ZnSnS_4 synthesized through a green and economic process. J Alloys Compd 509:9627–9630

[161] Zhou Y, Xi SQ, Sun CF, Wu HJ (2016) Facile synthesis of Cu_2ZnSnS_4 powders by mechanical alloying and annealing. Mater Lett 169:176–179

[162] Pani B, Pillai S, Singh UP (2016) Kesterite based thin film absorber layers from ball milled precursors. J Mater Sci Mater Electron 27:12412–12417

[163] Pareek D, Balasubramaniam KR, Sharma P (2016) Synthesis and characterization of kesterite $Cu_2ZnSnTe_4$ via ball-milling of elemental powder precursors. RSC Adv 6:68754–68759

[164] Pareek D, Balasubramaniam KR, Sharma P (2015) Synthesis and characterization of bulk Cu_2ZnSnX_4 (X: S, Se) via thermodynamically supported mechano-chemical process. Mater Charact 103:42–49

[165] Ritscher A, Just J, Dolotko O, Schorr S, Lerch M (2016) A mechanochemical route to single phase Cu_2ZnSnS_4 powder. J Alloys Compd 670:289–296

[166] Ritscher A, Hoelzel M, Lerch M (2016) The order–disorder transition in Cu_2ZnSnS_4—a neutron scattering investigation. J Solid State Chem 238:68–73

[167] Ritscher A, Schlosser M, Pfitzner A, Lerch M (2016) Study of the mechanochemical process to crystalline Cu_2ZnSnS_4 powder. Mater Res Bull 84:162–167

[168] Ma RX, Yang F, Li SN et al (2016) Fabrication of $Cu_2ZnSn(S, Se)(4)$(CZTSSe) absorber films based on solid-phase synthesis and blade coating processes. Appl Surf Sci 368:8–15

[169] Yang F, Ma RX, Zhao WS, Zhang XY, Li X (2016) Fabrication of Cu_2ZnSnS_4 (CZTS) absorber films based on different compound targets. J Alloys Compd 689:849–856

[170] Ritscher A, Franz A, Schorr S, Lerch M (2016) Off-stoichiometric CZTS: Neutron scattering investigations on mechanochemically synthesized powders. J Alloys Compd 689:271–277

[171] Tiwari A, Dhoble SJ (2016) Stabilization of ZnS nanoparticles by polymeric matrices: syntheses, optical properties and recent applications. RSC Adv 6:64400–64420

[172] Medintz IL, Uyeda HT, Goldman ER, Mattoussi H (2005) Quantum dot bioconjugates for imaging, labelling and sensing. Nat Mater 4:435–446

[173] Bujňáková Z, Dutková E, Zorkovská A et al (2017) Mechanochemical synthesis and in viro studies of chitosan-coated InAs/ZnS mixed nanocrystals. J Mater Sci 52:721–735. doi:10.1007/s10853-016-0366-x

[174] Bujňáková Z, Baláž P, Čaplovičová M, Čaplovič L, Kováč J, Zorkovská A (2015) Mechanochemical synthesis of InAs nanocrystals. Mater Lett 159:474–477

[175] Bujňáková Z, Baláž M, Zdurienčíková M et al (2017) Preparation, properties and anticancer effects of mixed As_4S_4/ZnS nanoparticles capped by Poloxamer 407. Mater Sci Eng C 71:541–551

[176] Tiwari JP, Shahi K (2007) Mechanochemically synthesized Ag_2S–Sb_2S_3 amorphous fast ionic conductors. Mater Sci Eng B 141:8–15

[177] Boldyrev VV, Boldyreva EV (2010) In: Delogu F, Mulas G (eds) Experimental and theoretical studies in modern mechanochemistry. Transworld Research Network, Trivandrum

[178] Suryanarayana C, Ivanov E, Boldyrev VV (2001) The science and technology of mechanical alloying. Mater Sci Eng A 304–306:151–158

[179] Filio JM, Kasai E, Ymetsu Y, Saito F, Chung HS (1994) Grinding of Ep dust and its effect on solubility of metal-compounds in water. J Chem Eng Jpn 27:492–497

[180] Rogach AL (2008) Semiconductor nanocrystal quantum dots. Springer, New York

[181] Hines MA, Guyot-Sionnest P (1996) Synthesis and characterization of strongly luminescing ZnS-Capped CdSe nanocrystals. J Phys Chem 100:468–471

[182] Smyder JA, Krauss TD (2011) Coming attractions for semiconductor quantum dots. Mater Today 14:382–387

[183] Chen HM, Zhen ZP, Todd T, Chu PK, Xie J (2013) Nanoparticles for improving cancer diagnosis. Mater Sci Eng R 74:35–69

[184] Nam J, Won N, Bang J et al (2013) Surface engineering of inorganic nanoparticles for imaging and therapy. Adv Drug Del Rev 65:622–648

[185] Geszke-Moritz M, Moritz M (2013) Quantum dots as versatile probes in medical sciences: synthesis, modification and properties. Mater Sci Eng C 33:1008–1021

[186] Wageh S, Ling ZS, Xu-Rong X (2003) Growth and optical properties of colloidal ZnS nanoparticles. J Cryst Growth 255:332–337

[187] Chen R, Li DH, Liu B et al (2010) Optical and excitonic properties of crystalline ZnS nanowires: toward efficient ultraviolet emission at room temperature. Nano Lett 10:4956–4961

[188] Mishra PR, Al Shaal L, Muller RH, Keck CM (2009) Production and characterization of Hesperetin nanosuspensions for dermal delivery. Int J Pharm 371:182–189

[189] Xu Y, Zhao WW, Xu R, Shi YM, Zhang B (2013) Synthesis of ultrathin CdS nanosheets as efficient visible-light-driven water splitting photocatalysts for hydrogen evolution. Chem Commun 49:9803–9805

[190] Liu J, Lu YF, Wu Q, Goyer RA, Waalkes MP (2008) Mineral arsenicals in traditional medicines: orpiment, realgar, and arsenolite. J Pharmacol Exp Ther 326:363–368

[191] Dilda PJ, Hogg PJ (2007) Arsenical-based cancer drugs. Cancer Treat Rev 33:542–564

[192] Baláž P, Sedlák J (2010) Arsenic in cancer treatment: challenges for application of realgar nanoparticles (a minireview). Toxins 2:1568–1581

[193] Baláž P, Nguyen AV, Fabián M et al (2011) Properties of arsenic sulphide As_4S_4 nanoparticles prepared by high-energy milling. Powder Technol 211:232–236

[194] Baláž P, Fabián M, Pastorek M, Cholujová D, Sedlák J (2009) Mechanochemical preparation and anticancer effect of realgar As_4S_4 nanoparticles. Mater Lett 63:1542–1544

[195] Bujňáková Z, Baláž P, Makreski P et al (2015) Arsenic sulfide nanoparticles prepared by milling: properties, free-volume characterization, and anti-cancer effects. J Mater Sci 50:1973–1985. doi:10.1007/s10853-014-8763-5

[196] Harder J (2015) Energy trend: advances in fine grinding and classification. Aufbereitungs-Technik/Miner Process 56:42–55

[197] Harder J (2012) Improved yields-trends in the grinding of non-ferrous metal ores. Aufbereitungs-Technik/Miner Process 7–8:49–62

[198] www.isamill.com (2017). Accessed 22 Jan

[199] Gock E, Vogt V, Baláž P (2008) In: Duo WD, Yao SC, Liang WF, Zhang LC, Long H (eds) Proceedings of the XXIV. International Mineral Processing Congress Science Press, Beijing

[200] Gock E, Kurrer KE (1999) Eccentric vibratory mills—theory and practice. Powder Technol 105:302–310

[201] Achimovičová M, Baláž P, Ohtani T et al (2011) Characterization of mechanochemically synthesized ZnSe in a laboratory and an industrial mill. Solid State Ion 192:632–637

[202] Achimovičová M, Baláž P, Ďurišin J et al (2011) Mechanochemical synthesis of nanocrystalline lead selenide: industrial approach. Int J Mater Res 102:441–445